

Searches for new physics in $t\bar{t}$ pair production at the Large Hadron Collider

Candidate

Antonella Succurro

Supervised by

Dr. Aurelio Juste Rozas

Institució Catalana de Recerca i Estudis Avancat

Institut de Física d'Altes Energies

Professore: Lei ha una qualche ambizione?

Nicola: Ma... Non...

Professore: E Allora vada via... Se ne vada dall'Italia. Lasci l'Italia finché è in tempo.
Cosa vuole fare, il chirurgo?

Nicola: Non lo so, non ho ancora deciso...

Professore: Qualsiasi cosa decida, vada a studiare a Londra, a Parigi... Vada in
America, se ha le possibilità, ma lasci questo Paese. L'Italia è un Paese da
distruggere: un posto bello e inutile, destinato a morire.

Nicola: Cioè, secondo lei tra poco ci sarà un'apocalisse?

Professore: E magari ci fosse, almeno saremmo tutti costretti a ricostruire... Invece
qui rimane tutto immobile, uguale, in mano ai dinosauri. Dia retta, vada via...

da La meglio Gioventù di M.T. Giordana (2003)

⁴ Introduccion

⁵

Contents

8	Introduction	ix
9	1 Going beyond the Standard Model	1
10	1.1 Building the Standard Model	1
11	1.2 New Physics Models predicting vector-like quarks	1
12	2 The ATLAS experiment at the Large Hadron Collider	3
13	2.1 The Large Hadron Collider at CERN	3
14	2.2 The ATLAS detector	7
15	2.2.1 Coordinate system	8
16	2.2.2 Magnets	10
17	2.2.3 Inner detector	10
18	2.2.4 Calorimeters	13
19	2.2.5 Muon spectrometer	17
20	2.3 Forward sub-detectors	18
21	2.4 Trigger system	19
22	2.4.1 Level 1 trigger	20
23	2.4.2 Level 2 trigger	21
24	2.4.3 Event filter	21
25	2.5 Data Quality	21
26	3 Monte Carlo simulation	23
27	3.1 Parton shower	23
28	3.2 Hadronization	23
29	3.3 Underlying-event	23
30	3.4 Generators	23
31	4 Event reconstruction	25
32	4.1 ID Tracks	25

33	4.2	Primary vertices	26
34	4.3	Energy clusters	27
35	4.4	Electrons	28
36	4.4.1	Additional requirement and corrections for analyses	29
37	4.5	Muons	30
38	4.5.1	Additional requirement and corrections for analyses	31
39	4.6	Jets	32
40	4.6.1	Additional requirement and corrections for analyses	33
41	4.6.2	b -tagging	34
42	4.7	Missing Transverse Energy	38
43	5	Searches for vector-like top partner pairs in the single lepton channel	39
44	5.1	General strategy for $T\bar{T}$ pairs searches	39
45	5.2	Data sample and common event preselection	39
46	5.3	Background and signal modeling	40
47	5.3.1	Monte Carlo simulated samples	41
48	5.3.2	Multi-jet background	44
49	5.4	Systematical uncertainties treatment	44
50	6	Preliminary search for $T\bar{T}$ pairs decaying to $Wb + X$	45
51	6.1	Boosted W reconstruction	45
52	6.2	Control regions	45
53	6.3	Event selection	45
54	6.4	Systematics	45
55	7	Preliminary search for $T\bar{T}$ pairs decaying to $Ht + X$	47
56	7.1	Control regions	47
57	7.2	Event selection	47
58	7.3	Systematics	47
59	8	Results	49
60	8.1	Combination	49
61		Conclusions	51
62		A	53
63		B	55
64	C	Search for $T\bar{T} \rightarrow Wb + X$ at $\sqrt{7}$ TeV	57
65		Bibliography	59

66 Introduction

67

68 The analyses presented in this dissertation have been performed analyzing data from
69 proton-proton (p-p) collisions at the center of mass energy $\sqrt{s} = 8$ TeV recorded during the
70 year 2012 at the ATLAS experiment [\[1\]](#).

72 Going beyond the Standard Model

73

74 The Standard Model (SM) of particle physics is the most successful, beautiful and
75 precise theory describing the interactions between fundamental particles. Its validity has
76 been tested by precision measurements at the Large Electron-Positron Collider (LEP) at
77 CERN and confirmed by the observation of all the particles it predicts, including the Higgs-
78 like boson discovered at the Large Hadron Collider (LHC) in July of 2012 which up to now
79 behaves as expected from the SM.

80 What makes the SM “only” and effective theory is the fact that unstabilities appear at
81 high energy scales of the order of the Planck mass. In this Chapter we will show

82 1.1 Building the Standard Model

83 1.2 New Physics Models predicting vector-like quarks

84 [2, 3]

The ATLAS experiment at the Large Hadron Collider

88

The time when particle physics experiments could fit in one's loft is well passed, if it ever existed. The reason is simple, as the deeper we want to investigate matter, the highest the energy we need. According to the Standard Model, we now know all the particles composing ordinary matter present in nature, so if we want to see something new, we need to produce it. The way to do it is suggested by one of the fundamental principles of relativity, $E = mc^2$, according to which we can smash massive particles and observe what other kind of matter comes out of the available energy. Soon enough after the discovery of the muon, after observing all the observable from cosmic rays, physicists started to do that using particle accelerators, the last of them in history being the Large Hadron Collider.

The Large Hadron Collider, built to collide protons at a center of mass energy of 14 TeV, is the world's highest energy particle accelerator, overcoming the Tevatron proton-antiproton collider where the top quark was discovered in 1995 [4, 5]. The ATLAS experiment is one of the collaborations that take advantage of the collisions provided by the Large Hadron Collider, and has been conceived to pursue a challenging physics program with, at the head of the list, the discovery of the Higgs boson, achieved in 2012 [6].

In the following Chapter we will briefly describe the main features of the accelerator and with some more details the ATLAS detector, both located at the CERN laboratories in Geneva, Switzerland.

2.1 The Large Hadron Collider at CERN

The LHC program was approved by CERN Council in 1994, followed by the approval of the four main experiments: ATLAS [1] and CMS [7] in 1996; ALICE [8] in 1997; LHCb [9] in 1998. Works towards the installation of the most powerful particle accelerator of the world started when the Large Electron Positron Collider (LEP) was dismantled in 2000 to give up its place in the tunnel to the LHC, which was then fully operational by 2008.

The ATLAS experiment [1] is situated at Point 1 along the Large Hadron Collider

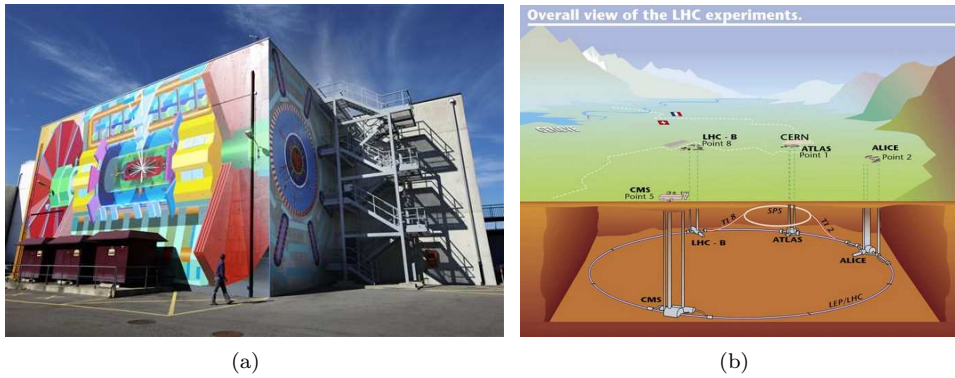


Figure 2.1: Left: View of Point 1, just above the ATLAS cavern, with a mural painting of the detector, reproduced at a scale of about 1:3 by artist Josef Kristofletti¹. Right: A drawing of the LHC complex.

(LHC) [10] 27 km long ring (Figure 2.1). The accelerator tunnel can reach an underground depth of 175 meters and is spread between Swiss and French territory, while the cave where ATLAS is allocated is about 100 meters underground in the CERN Swiss site of Meyrin.

The collider accelerates protons up to 4 TeV, but is designed to reach 7 TeV per beam when it will be operated at his full potential. This energy is achieved through various steps, shown in Figure 2.2. To start with, protons are extracted from Hydrogen gas and injected in the first machine, the linear accelerator LINAC2 that starts the acceleration chain. When protons reach an energy of 50 MeV they are injected into the Proton Synchrotron Booster (PSB) and accelerated up to the energy of 1.4 GeV. The second circular accelerator, the Proton Synchrotron (PS) brings the energy of the protons to 25 GeV previous to injecting them into the last machine before the LHC, the Super Proton Synchrotron (SPS). Protons of 450 GeV finally enter the LHC where they are boosted to energies of up to 4 TeV. The four main LHC experiments are shown on the collider ring.

The LHC is composed of eight arcs 2.7 km long, each of which contains 154 dipole magnets, whose function is to bend the beams along the circular trajectory, and 49 quadrupole magnets, that focus the beam. These superconducting magnets operate at a temperature of 1.9 K, maintained by means of liquid Helium vessels. Eight insertions are placed inbetween the arches. Each insertion has a specific role that characterizes its design and can be injection, beam dumping, beam cleaning, or “physics”, i.e. make the beams collide within an experiment.

First proton beams were circulated on 10th September 2008 and right on the verge of getting the first collisions at a center of mass energy $\sqrt{s} = 900$ GeV nine days later, an electrical connection joining superconducting wires of a dipole and a quadrupole failed. This caused the release of liquid Helium in the insulating vacuum, resulting in an explosion that severely damaged the machine. After more than one year devoted to repair the damage and consolidate the security, on 30th November 2009 the LHC became the world’s highest energy particle accelerator²:

¹More info at: <http://www.atlas.ch/mural/>.

²<http://press.web.cern.ch/press/PressReleases/Releases2009/PR18.09E.html>

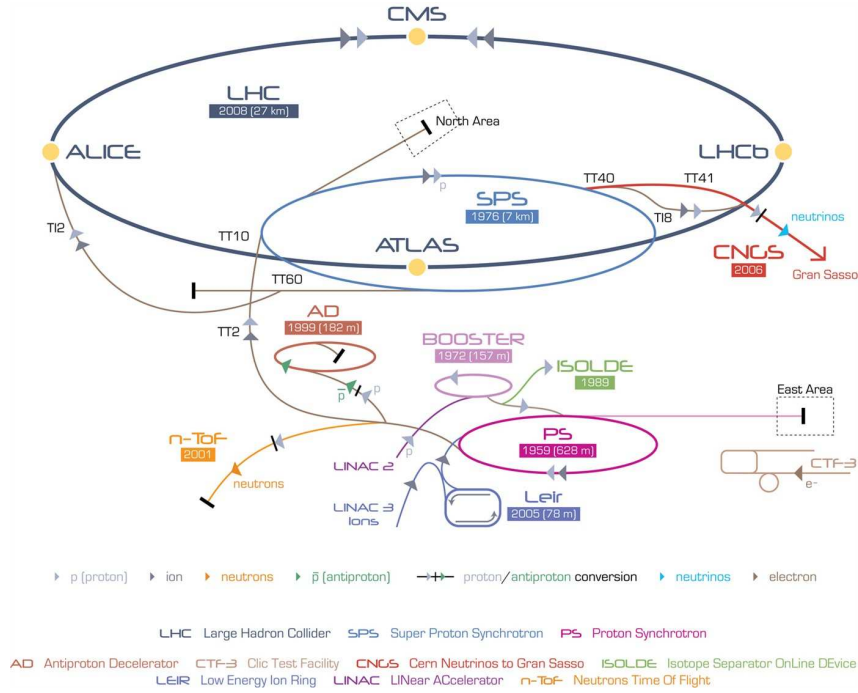


Figure 2.2: A schematic showing the accelerator complex at CERN.

141 Geneva, 30 November 2009. CERN's Large Hadron Collider has today become the
 142 world's highest energy particle accelerator, having accelerated its twin beams of protons
 143 to an energy of 1.18 TeV in the early hours of the morning. This exceeds the previous
 144 world record of 0.98 TeV, which had been held by the US Fermi National Accelerator
 145 Laboratory's Tevatron collider since 2001. It marks another important milestone on the
 146 road to first physics at the LHC in 2010.

One of the main characteristics for an accelerator is the luminosity, the instantaneous luminosity \mathcal{L} being defined as

$$\mathcal{L} \times \sigma = \frac{dN}{dt} = f \times n \frac{N_1 \times N_2}{A} \times \sigma. \quad (2.1)$$

147 Here dN/dt is the event rate of a certain process and σ is its cross section. This rate is
 148 directly proportional to the frequency f , the number of bunches n and the number of
 149 particles in the two bunches N_1, N_2 , and inversely proportional to the beam cross-section
 150 A . The instantaneous luminosity is measured by dedicated subdetectors that are described
 151 in Section 2.3.

Integrating over the accelerator active time (a "fill", when stable beams are kept colliding) gives the *integrated luminosity*, relating the total number of produced events N_{tot} to the cross-section:

$$\int \mathcal{L} dt = \frac{N_{tot}}{\sigma}. \quad (2.2)$$

152 In 2010 ATLAS collected about 45 pb^{-1} of p-p collision data at $\sqrt{s}=7 \text{ TeV}$, and in 2011
 153 reached about 5 fb^{-1} of the same data. In 2012, with $\sqrt{s}=8 \text{ TeV}$ collisions, LHC reached

Parameter	designed	2010	2011	2012
Beam energy (TeV/c)	7	3.5	3.5	4
Beta function β^* (m)	0.55	2.0/3.5	1.5/1.0	0.6
Max. No. bunches/beam	2808	368	1380	1380
Max. No. protons/bunch	1.15×10^{11}	1.2×10^{11}	1.45×10^{11}	1.7×10^{11}
Bunch spacing (ns)	25	150	75/50	50
Peak luminosity ($\text{cm}^{-2}\text{s}^{-1}$)	1×10^{34}	2.1×10^{32}	3.7×10^{33}	7.7×10^{33}
Emittance ε_n (μrad)	3.75	2.0	2.4	2.5
Max. $\langle \mu \rangle$	19	4	17	37

Table 2.1: Overview of some parameters for the LHC performance comparing the design values with their time evolution during the first long run operation in 2010-2013 [11].

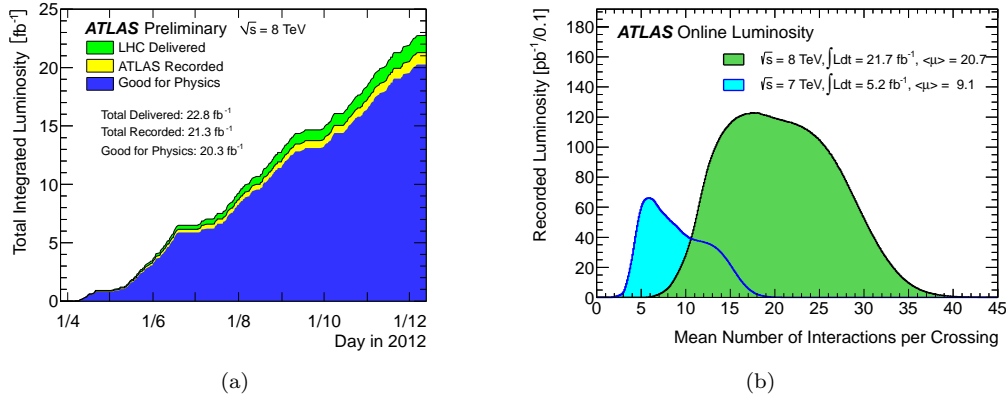


Figure 2.3: (a) Total integrated luminosity versus time delivered by the LHC to ATLAS (in green), recorded by the experiment (in yellow) and selected as “good data” for analysis (in blue) for p-p collisions at $\sqrt{s}=8 \text{ TeV}$. (b) Mean number of interactions per beam crossing during 2011 and 2012 LHC runs, where $\mu = \mathcal{L} \times \sigma_{\text{inelastic}}/f$ depends on the instantaneous luminosity \mathcal{L} , the p-p inelastic cross section $\sigma_{\text{inelastic}}$ and the revolution frequency f . [12]

154 a peak luminosity of $7.7 \times 10^{33} \text{ cm}^{-2}\text{s}^{-1}$ which is more than half the design luminosity, as
 155 shown in Table 2.1 together with other parameters relevant for the accelerator performance.
 156 Over 2012, the last year of data taking before the long shutdown³, ATLAS collected about
 157 20 fb^{-1} of p-p collision data at $\sqrt{s}=8 \text{ TeV}$. Figure 2.3(a) shows the delivered luminosity from
 158 the start of stable beams until beam dump and the luminosity recorded by ATLAS during
 159 stable beam conditions, the difference with respect to the delivered luminosity being due to
 160 Data Acquisition (DAQ) inefficiencies. Of the recorded luminosity, only a part is usable for
 161 analysis, and is what is called “good data”, i.e. the data that satisfy Data Quality (DQ)
 162 requirements assessed after reprocessing (see Section 2.5).

163 In order to increase the luminosity LHC operates with a high number of protons per
 164 bunch as well as a high number of bunches per beam and reduces the inter-bunch latency

³LHC terminated the p-p program at the end of 2012, operated proton-heavy ion collisions for two months at the beginning of 2013 and then stopped for what is called the first long shutdown. During this two-years time the accelerator and the experiments as well will undergo substantial maintenance and upgrade works, in order to be re-operated in 2015 with higher performance at a higher center of mass energy for particle collisions.

time. This overall defines a set of challenges that physics analysis will face associated to the high luminosity. Even at the detector design stage, the high frequency of collision environment foreseen influenced the choice of radiation resistance material for the experiment sub-systems. Concerning directly the physics instead, the main problematic is *pile-up*.

Pile-up events are distinguished between *in-time* and *out-of-time* pile-up. The first ones come from the multiple inelastic scatterings of protons in the same bunch, as if we consider a cross-section of 80 mb at the nominal luminosity of $10^{34} \text{ cm}^{-2}\text{s}^{-1}$ the number of events per second will be something like a billion. This translate, at a collision frequency of one crossing every 25 ns, to about 20 interactions per crossing that will be detected simultaneously. A useful observable to estimate in-time pile-up is the number of reconstructed primary vertices (see Section 4.2) N_{PV} . In addition, on the other hand, the inter-bunch time interval is so short that the electronics reading the detector might not keep up with the frequency of collisions, leading to the cumulation of events that happened in different beam crossings. This is the effect we refer to as out-of-time pile-up, and a good estimator for it is the average number of p-p interactions per bunch crossing at the time of the event, $\langle \mu \rangle$, which recalling Equation 2.1 is defined as:

$$\langle \mu \rangle = \frac{LA}{nf}, \quad (2.3)$$

with L being the average instantaneous luminosity over a time period $\Delta t \gg 600$ ns. The maximum values reached by the variable $\langle \mu \rangle$ during the three years of data taking are reported in Table 2.1.

Finally, ATLAS makes use of a three-level trigger system (described in Section 2.4) to identify and record only the events of interest, while the pile-up issues are dealt with at the analysis reconstruction level.

2.2 The ATLAS detector

ATLAS (A Toroidal LHC ApparatuS) [1] is a general purpose experiment aimed at exploring a vast range of physics scenarios and designed to measure the particles produced in p-p collisions at the LHC at unprecedented energies and instantaneous luminosities. It is the biggest detector of its kind ever built (it's 46 m long and 25 m high) is characterized by a full coverage of the space around the p-p interaction point and complete containment of the particles produced in the collision. Different subsystems are layered concentrically one after the other, each of them pursuing a specific task. Right around the interaction point (IP) where the LHC makes protons collide there is the Vertex Detector, reconstructing charged particles trajectories that are bent by the first solenoid magnet surrounding the Vertex Detector. Particles going through it then encounter the two calorimeter systems, the Electromagnetic and the Hadronic one. Muons are the only particles that will pass the calorimeters material (beyond neutrinos) and a dedicated Muon Spectrometer is the last piece of detector, embedded in a huge toroidal magnet. The detector complex is presented as a schematic in Figure 2.4, and a drawing of particle detection in the various subdetector systems is shown in Figure 2.5.

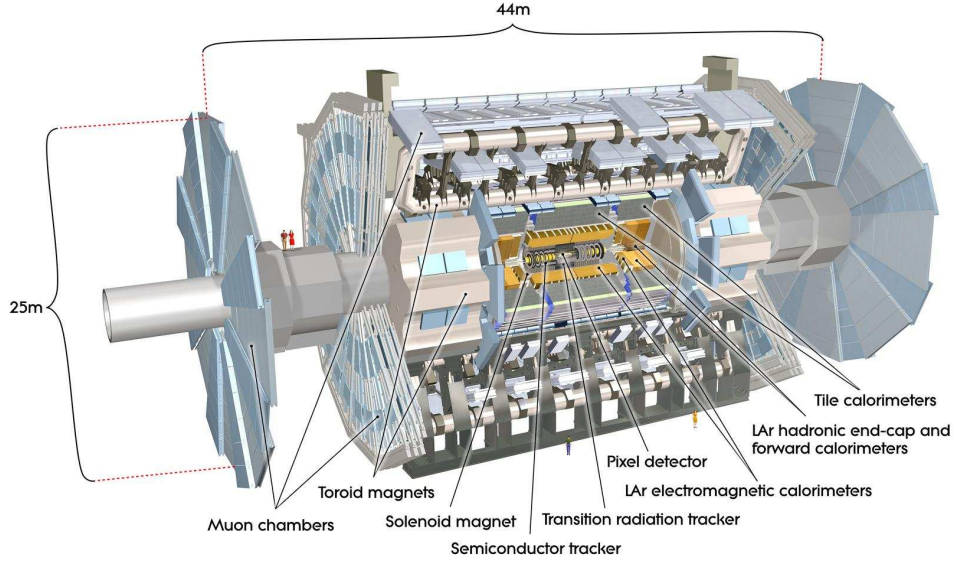


Figure 2.4: Schematic drawing of the ATLAS experiment. The detector subsystem are indicated as well as the total dimensions.

2.2.1 Coordinate system

Protons from the two circulating beams are made to collide in the center of the ATLAS detector, in the region that takes the name of Interaction Point (IP). The IP is taken as the origin of a three dimensional XYZ right-handed coordinate system. The Z axis is tangent to the trajectory of the beams while the XY plane is perpendicular to it and defines a symmetry plane for the detector, dividing it into the *A* and *C* sectors, respectively in the positive and negative Z semi-axes. Figure 2.6(a) shows a schematic of the coordinate system.

In terms of polar coordinates, the Z axis is again along the beam axis and in the transverse plane the *R* and ϕ coordinates are defined with ϕ ranging between $-\pi$ and $+\pi$ with respect to the X axis. In terms of spherical coordinates (see Figure 2.6(b)), the radial vector *R* originates from the IP, the azimuth ϕ is the same as the polar angle ϕ , and the polar angle θ is measured with respect to the Z axis and ranges between 0 and π .

Since the interaction initial energy is unknown, being dependent on the parton distribution functions for the proton energy, it is useful to define the transverse component of variables of interest⁴ like the energy and the momentum, being taken as the projection on the XY plane:

$$E_T = E \sin \theta, \quad p_T = p \sin \theta. \quad (2.4)$$

Another common variable used at hadron colliders to describe the polar distribution and

⁴These quantities transverse initial value will be, indeed, zero, as the protons are accelerated along the Z axis.

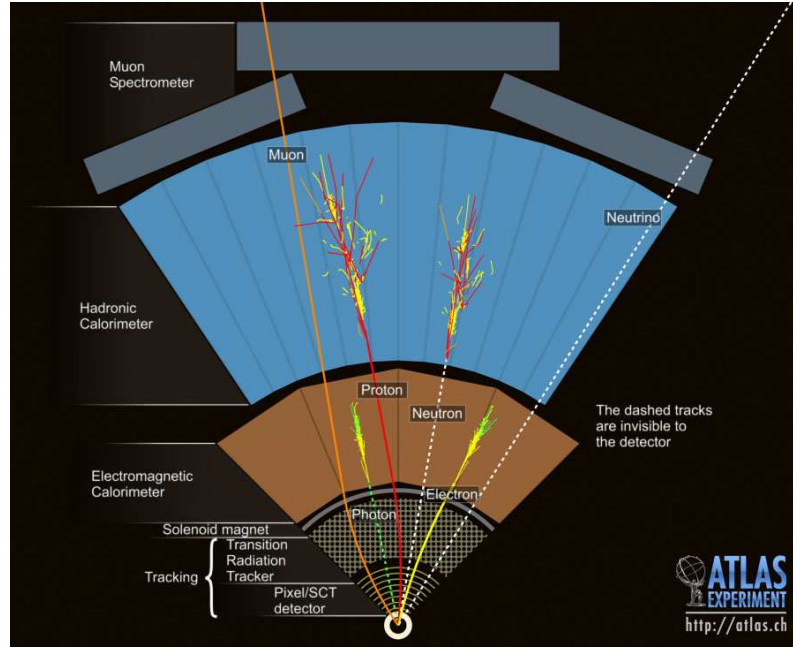


Figure 2.5: Drawing of the detection of particles going from the interaction point through the whole detector.

preferred to the simple polar angle θ is the pseudorapidity η :

$$\eta \equiv -\ln \left(\tan \frac{\theta}{2} \right); \quad (2.5)$$

which, for relativistic regimes, is equal to the rapidity y :

$$y \equiv \frac{1}{2} \ln \left(\frac{E + p_z}{E - p_z} \right); \quad (2.6)$$

and Δy and $\Delta \eta$ are Lorentz invariant. The pseudorapidity is preferred to the rapidity as it does not require knowing the particle mass but only its polar position. The distance between two particles is often referred to in terms of ΔR :

$$\Delta R = \sqrt{(\Delta \eta)^2 + (\Delta \phi)^2}. \quad (2.7)$$

207 Figure 2.6(b) shows how different pseudorapidity regions are named. Particles along the
 208 Z axis have a pseudorapidity $|\eta| = \infty$, particles along the Y axis have a pseudorapidity
 209 $|\eta| = 0$. ATLAS has an excellent hermeticity and is able to cover pseudorapidity regions up to
 210 $|\eta| = 4.9$. Typically, physics analysis consider objects in the pseudorapidity region $|\eta| < 2.5$.
 211 For a quick visualization of the correspondence in terms of polar angle distribution, some
 212 pseudorapidity values are reported in Table 2.2.

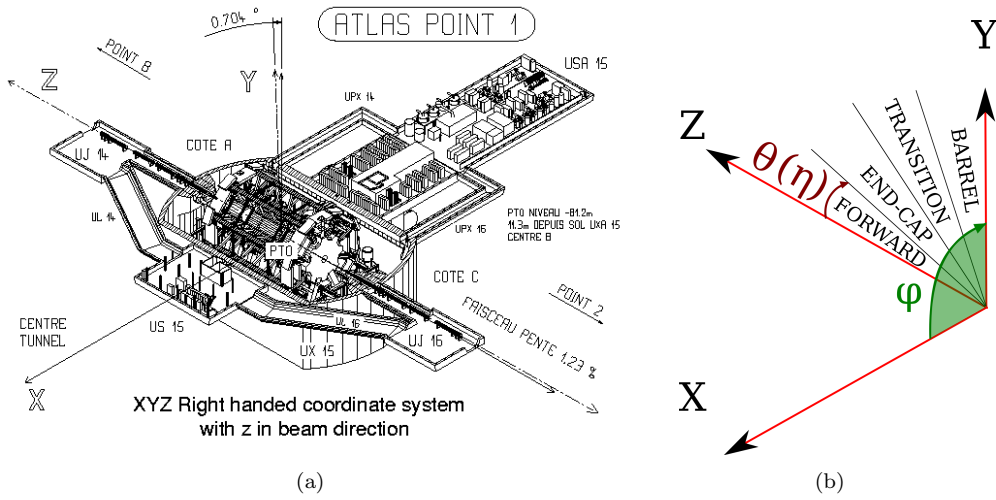


Figure 2.6: (a) Drawing of the ATLAS experiment with the cartesian coordinate system. The positive X axis points towards the center of the LHC ring. The positive Z axis points towards the anti-clockwise circulating direction of beam 2. (b) Simple schematic showing the spherical coordinates and the region definition in terms of the absolute value of the pseudorapidity η . These regions are symmetrical with respect to the transverse XY plane.

θ	0°	5°	10°	20°	30°	45°	60°	80°	90°
η	∞	3.13	2.44	1.74	1.31	0.88	0.55	0.175	0

Table 2.2: Pseudorapidity vs polar angle values.

2.2.2 Magnets

ATLAS is provided with four superconducting magnets that allow the measurement of charged particles momenta by curving their trajectory.

A central solenoid, 5.3 m long and 2.4 m in diameter, sits around the inner detector and produces a 2 T magnetic field along the direction parallel to the beam axis. It is only 45 mm thick (equivalent to 0.66 radiation lengths X_0) and is cooled with liquid Helium, sharing the cryostat with the electromagnetic calorimeter.

Paired to the muon spectrometer, the superconducting air-core toroid magnet (Figure 2.7) has an open structure with eight superconducting toroidal coils in the barrel part (each 25.3 m long, located at the outer diameter of 20.1 m) and two end-cap systems made of eight coils. The field strength varies strongly with ϕ : in the barrel region ($|\eta| < 1.4$) is 1.5-5.5 Tesla-m; in the end-caps ($1.6 < |\eta| < 2.7$) 1-7.5 is Tesla-m. Such configuration of the magnets gives a field orthogonal to the muons trajectory.

2.2.3 Inner detector

The Inner Detector (ID) is the subsystem closest to the IP and tracking charged particles arising from collisions allows for the measurement of their momentum and vertex reconstruction with excellent resolution. At the design choices level, radiation resistance had to be taken into account, as well as reducing the amount of material to be placed in front of

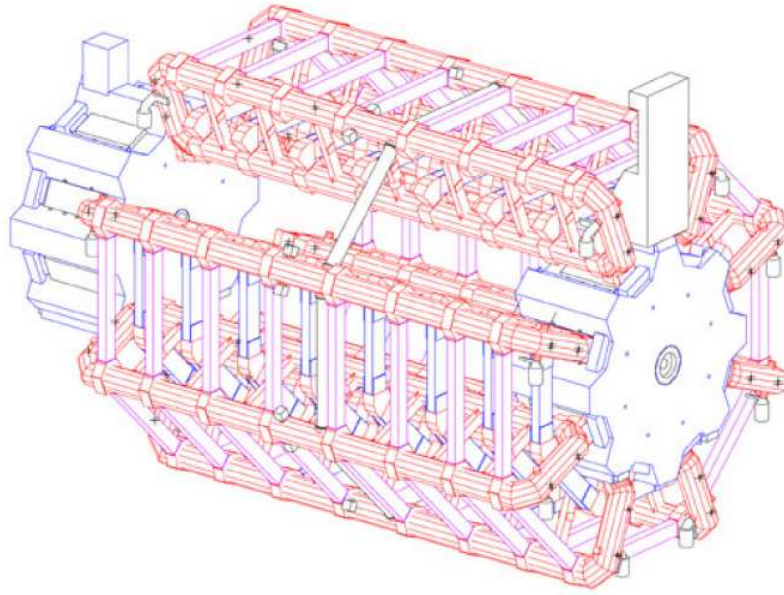


Figure 2.7: Toroidal magnet system.

the calorimeters to avoid spoiling the energy measurement. This quantity varies between 0.5 and $2.5 X_0$ depending on the pseudorapidity region, most of it coming from supporting equipment. This material is responsible for photon conversions and electron bremsstrahlung.

The ID is surrounded by the central solenoid magnet (Section 2.2.2) and is composed by three subsystems, from the closest to the furthest from the IP: the pixel detector, the SemiConductor Tracker (SCT) and the Transition Radiation Tracker (TRT).

Pixel detector

The first subsystem covers the region $|\eta| < 2.5$ and is composed by three cylindrical layers in the barrel region, each of them distant from the beam by 50.5 mm, 88.5 mm and 122.5 mm respectively, and by three concentric discs in the end-cap region, each of them distant from the beam by 49.5 mm, 58.0 mm and 65.0 mm respectively. Each silicon pixel has a size of $50 \times 400 \mu\text{m}^2$ and is $250 \mu\text{m}$ thick, with in total ~ 80.4 million readout channels to achieve a very fine granularity. The precision is of $10 \mu\text{m}$ in $R\phi$ and $115 \mu\text{m}$ in Z and R in the barrel and end-cap region respectively.

The very first layer is called B -layer as, thanks to its position really close to the IP, allows for the reconstruction of secondary vertices associated with the production of short lived particles such as B -hadrons. This information is very useful to identify jets originating from the fragmentation of b quarks.

Semiconductor tracker

After the three layers of pixel detectors, come four layers of silicon strip detectors. The SemiConductor Tracker (SCT) also covers the region $|\eta| < 2.5$ with a barrel and end-cap

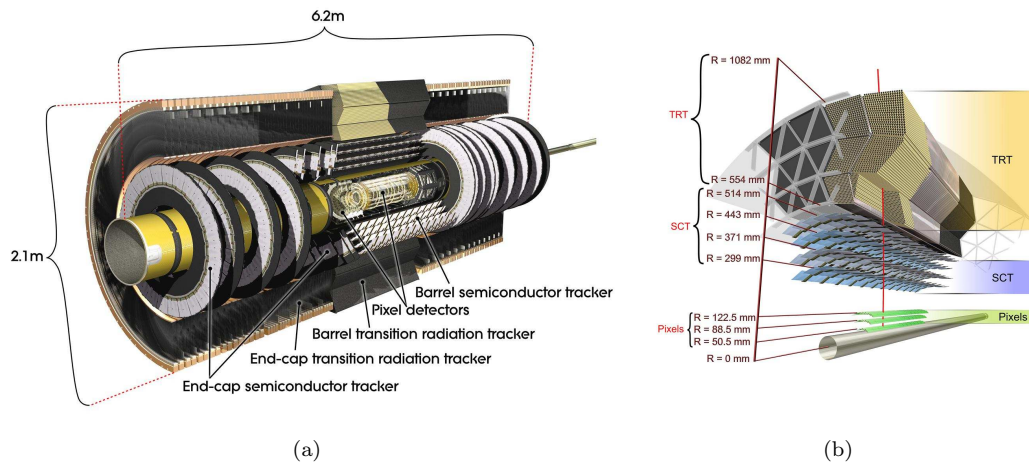


Figure 2.8: (a) Schematic of the ID system. (b) Detailed schematic of the barrel section of the ID showing the three subsystems and reporting the distance to the center of the beam pipe.

design similar to the pixel detector one, being composed by eight silicon strips (two per layer) 128 mm long and 80 μm large. It makes use of ~ 6.3 millions readout channels and the resolution achieved is of 17 μm in $R\phi$ and 580 μm in Z (R) in the barrel (end-cap) region.

By allowing for four redundant position measurements⁵, the SCT contributes mainly to the momentum reconstruction.

Transition Radiation Tracker

In order to reduce the amount of material in front of the calorimeters, and to reduce the construction costs as well, in the third subsystem the semiconductor technology has been substituted with straw detectors. The Transition Radiation Tracker (TRT) consists of thin proportional chambers made of straw polyimide drift tubes, 4 mm in diameter. The drift tubes are filled with a gas mixture composed of: 70% Xenon, 27% Carbon Dioxide, 3% Oxygen. The anode collecting the electrons from the ionized gas at the passage of the charged particle is made of tungsten covered in gold.

In the barrel region the tubes are 144 cm long and placed parallel to the beam axis, while in the end-cap region they are 37 cm long and positioned radially in wheels, with layers of radiator foils alternated to layers of straws. The resolution achieved is of 130 μm in $R\phi$ and $Z\phi$ in the two regions respectively. The covered pseudorapidity region is of $|\eta| < 2.0$ and the readout is composed by ~ 351000 channels.

About 36 measurements per track are taken, and since each channel provides two independent thresholds per hit, it is possible to discriminate between electrons and pions, since the former will more likely reach the high threshold.

In the end, the combination of the three ID subsystems gives very precise $R\phi$ and Z measurements, as well as good track pattern recognition. The resolution on the transverse

⁵One of the coupled layers is rotated of 40mrad with respect to the other, which is parallel to the axis, giving a small stereo angle for a redundancy in the ϕ coordinate measurement.

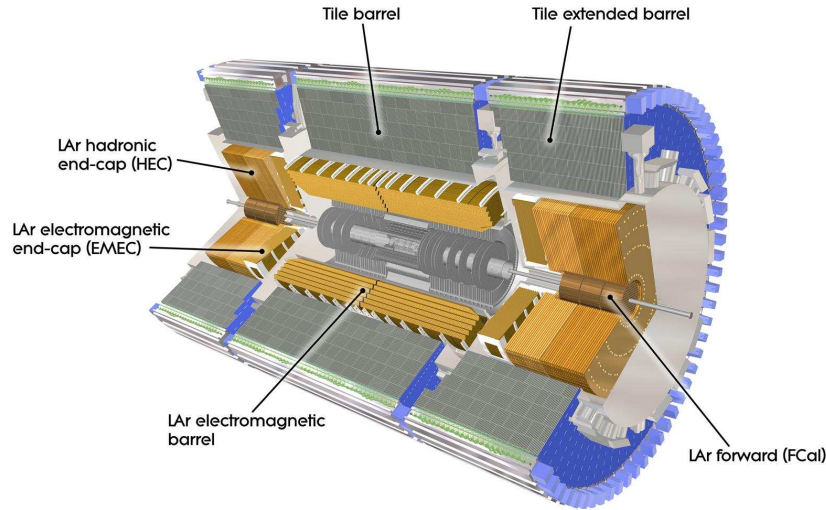


Figure 2.9: Schematic of the calorimeter complex of the ATLAS detector.

momentum, measured with cosmic muon calibration runs [13], is:

$$\frac{\sigma_{p_T}}{p_T} = P_1 \oplus P_2 \times p_T, \quad (2.8)$$

where $P_1 = 1.6 \pm 0.1\%$ and $P_2 = (53 \pm 2) \times 10^{-5} \text{ GeV}^{-1}$. This means a resolution of $\sim 1.6\%$ for tracks with $p_T \sim 1 \text{ GeV}$ and $\sim 50\%$ for tracks with $p_T \sim 1 \text{ TeV}$.

2.2.4 Calorimeters

Particles leaving the ID and surviving the crossing of the central solenoid magnet will face the calorimeter system, depicted in Figure 2.9. The full system is characterized by a coverage in pseudorapidity up to $|\eta| < 5$ and an almost full coverage in ϕ . With its $22 X_0$ and $24 X_0$ radiation lengths of material in the barrel and end-cap regions respectively it is also able to stop most of the non-muon particles from the interaction. Besides particles energy measurement, the calorimeters provide particle identification information, discriminating electrons, photons and jets, and the determination of the missing transverse energy.

Different technologies are used in the barrel, end-cap and forward regions for both the electromagnetic and the hadronic calorimeters. All of them are sampling calorimeters, with a dense medium acting as absorber to stop particles and start showers, and an active material to detect the signal from ionization. For the electromagnetic calorimeters and the forward hadronic calorimeter liquid argon is used as active medium, while the barrel and extended-barrel hadronic calorimeter uses scintillating tiles. The liquid argon is cooled at a temperature of about 88 K, with the use of two sets of cryostats: the barrel electromagnetic calorimeter shares the cryostat with the central solenoid; the end-cap and forward electromagnetic calorimeter and the hadronic end-cap calorimeter share a cryostat in the forward region.

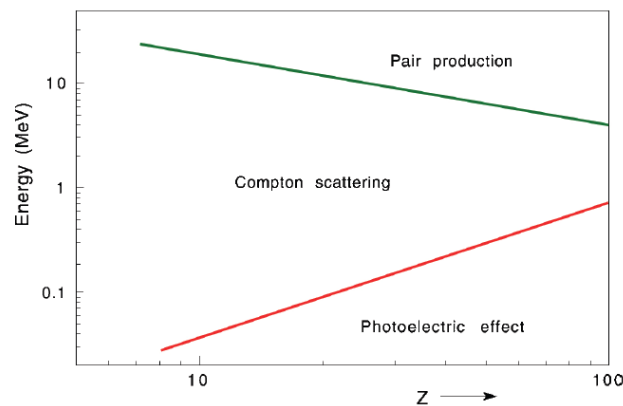


Figure 2.10: Domains in term of photon energy and Z number of the absorber material in which photoelectric effect, Compton scattering and pair production are the favorite processes for energy loss [14].

297 Particles interact both with the passive and active material, but only the energy released
 298 in the active samples will be detected. The processes involved in the shower formation
 299 are several and mainly electromagnetic. Photons in matter can undergo the photoelectric
 300 effect, Compton scattering and $\gamma \rightarrow e^+e^-$ pair formation. The general contribution of these
 301 processes depends both on the photon energy and on the atomic number Z of the material,
 302 and is shown in Figure 2.10. Electrons and positrons can ionize atoms and molecules,
 303 produce bremsstrahlung $e^\pm \rightarrow e^\pm + \gamma$ and emit Cerenkov radiation. Unless the calorimeter
 304 has been specifically designed for it, Cerenkov radiation does not contribute much, while
 305 ionization is the main process for energies up to ~ 100 MeV, where bremsstrahlung starts
 306 to dominate.

307 In general, these cascade of events continues until a certain threshold is reached, and
 308 the final number of particles produced is proportional to the energy of the first particle
 309 originating the shower.

310 Also hadrons interact with matter, either ionizing it (if charged) or by nuclear inter-
 311 actions. The problem of the latter process is that this energy release is often not directly
 312 detectable, like in nuclear breakups and excitations, and is therefore called “invisible energy”.
 313 Secondary hadrons will be produced, forming the hadronic part of the shower, but sooner or
 314 later something like $\pi^0 \rightarrow \gamma\gamma$ will happen and the shower will develop electromagnetically
 315 further on.

316 The average fraction of electromagnetic and hadronic shower components is a charac-
 317 teristic of the sampling calorimeter and depends on the choice of the passive and active
 318 material and on the design. Calorimeters are said to be *non-compensating* if, like the AT-
 319 LAS calorimeters, the detection of hadronic showers is less efficient than the one of elec-
 320 tromagnetic showers. Calorimeters with a similar response for the two components are
 321 called *compensating*, while calorimeters more efficient when revealing hadronic showers are
 322 *over-compensating*.

The performance for the energy resolution is parametrized by the following formula:

$$\frac{\sigma_E}{E} = \frac{S}{\sqrt{E}} \oplus \frac{N}{E} \oplus C, \quad (2.9)$$

where the terms of the sum correspond, respectively, to a “stochastic” term related to how shower develops in the sampling calorimeter; to a “noise” term including the contribution from electronic noise and pile-up energy fluctuation; to a systematic term that depends on calibration, shower containment, inactive material and on the linearity of the response as well.

The goal energy resolution for the liquid argon calorimeters is [15]:

$$\frac{\sigma_E}{E} = \frac{10\%}{\sqrt{E}} \oplus \frac{170 \text{ MeV}}{E} \oplus 0.7\%, \quad (2.10)$$

while for the hadronic barrel calorimeter is [16]:

$$\frac{\sigma_E}{E} = \frac{50\%}{\sqrt{E}} \oplus 5\%. \quad (2.11)$$

Test-beam runs to measure the response of the two calorimeters to electrons and single pions respectively have shown results comparable to the goal resolutions.

Electromagnetic calorimeter

The electromagnetic calorimeter, also called LAr calorimeter (from Liquid Argon, the active material), can measure electrons and photons energies in the range from 50 MeV to 3 TeV. In the barrel region it is referred to as EMB (ElectroMagnetic Barrel), is divided into two identical semi-barrels EMBA and EMBC separated at Z=0 by a 6 mm gap and covers the pseudorapidity region $|\eta| < 1.475$. Two end-cap detectors (EMEC, ElectroMagnetic End-Cap), divided into two coaxial wheels, cover the pseudorapidity regions $1.375 < |\eta| < 3.2$. A pre-sampler, extended over $|\eta| < 1.8$, stands in front of the EMB and allows for the measurement of the energy the particles lost before reaching the EMB i.e. crossing the material of the ID, the central solenoid and the cryostat.

Three longitudinal samples in the EMB are designed for different tasks. The first sample, $4.3X_0$ long, is finely segmented in η to precisely measure the direction in pseudorapidity of the particles with thin readout strips of $\Delta\eta \times \Delta\phi = 0.0031 \times 0.098$. This helps for photon/ π^0 discrimination and as well for separate close-by γ s from π^0 decay. The second sample, $16X_0$ long, contains the bulk of electrons and photons energy deposit. It is divided in towers with dimension $\Delta\eta \times \Delta\phi = 0.025 \times 0.0245$ and provides the position measurement of the cluster. The 95% of the energy of the shower is deposited in a matrix of 3×7 towers $\Delta\eta \times \Delta\phi$. The third sample, $2X_0$ long, is coarsely segmentes and collects the last bit of the longitudinal development of the electromagnetic showers. Towers in this region have a dimension of $\Delta\eta \times \Delta\phi = 0.05 \times 0.0245$.

Also the EMEC is divided in three longitudinal samples (two in the region $1.375 < |\eta| < 1.5$), and besides the lead, also the thickness of the liquid argon layers are varied in the radial direction.

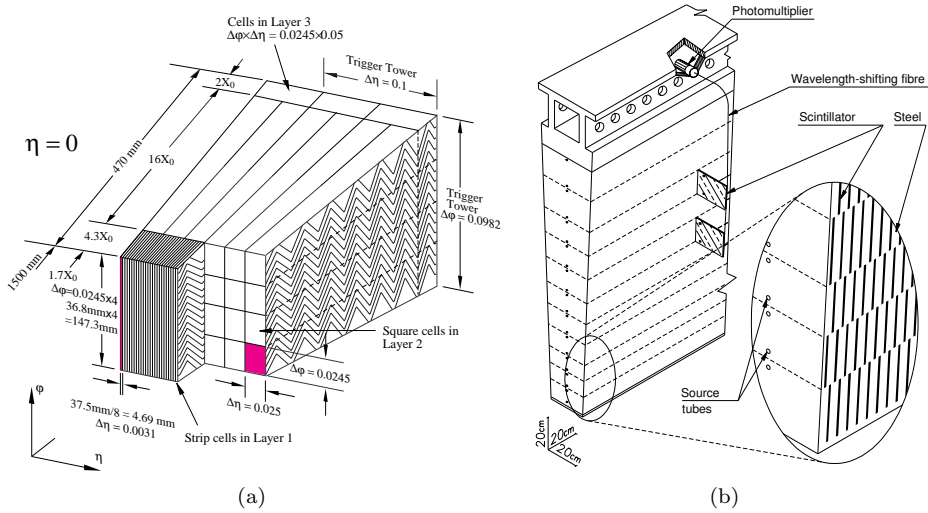


Figure 2.11: (a) Schematic drawing of a module of the Electromagnetic barrel calorimeter. (b) Schematic drawing of a module of the Hadronic barrel calorimeter.

The absorbing material is lead shaped into an accordion geometry to achieve full symmetry in ϕ , as shown in the drawing of Figure 2.11(a). Signal from the ionization produced in the liquid argon is collected by an electrode in the middle of the active material region, fixed into a honeycomb structure.

The thickness of the absorber layers depend on the pseudorapidity in order to make particles entering the system with different incident angles cross the same amount of material.

Hadronic calorimeters

Hadronic showers have typically a much longer shape than electromagnetic ones, and need therefore in general more interaction lengths of material to be fully contained. Hadronic calorimeters are therefore designed to completely absorb high-energy hadrons, which will deposit only some (small) part of their energy in the electromagnetic calorimeter.

Hadronic barrel calorimeter

The hadronic calorimeter in the barrel and extended barrel region, going up to $|\eta| < 1.7$, is made of scintillating tiles as active material with lead as absorber and is commonly referred to with the name of TileCal. The light in the ultraviolet range that is generated in the tiles is collected through wavelength shifting optical fibre (Figure 2.11(b)).

TileCal sits just after the electromagnetic calorimeter and measures the energy and position of jets and isolated hadrons. It is divided in depth in three layers with varying length (1.4, 4.1, 1.8 hadronic interaction lengths λ in the barrel and 1.5, 2.6, 3.3 λ in the extended barrel) and segmentation ($\Delta\eta \times \Delta\phi = 0.1 \times 0.1$ in the first two layers, $\Delta\eta \times \Delta\phi = 0.2 \times 0.1$ in the third), and in 64 slices in ϕ , each of $\Delta\phi \sim 0.1$.

The readout channels are grouped into cells that form a pseudo-projective geometry in η .

Hadronic end-cap calorimeter

The Hadronic End-Cap calorimeters (HEC) use copper as passive material and liquid argon as active material, chosen for its radiation hardness in a region ($1.5 < |\eta| < 3.2$) exposed to a significant amount of particle flux. Each HEC is composed by two independent wheels with granularity varying with η : in $1.5 < |\eta| < 2.5$ $\Delta\eta \times \Delta\phi$ is 0.1×0.1 in the first two longitudinal layers, 0.2×0.1 in the last one; in $2.5 < |\eta| < 3.2$ $1.5 < |\eta| < 2.5$ $\Delta\eta \times \Delta\phi = 0.2 \times 0.2$ in all the three samples.

The HECs collect the energy from particles that are not completely contained in the EMECs and in particular are used to reconstruct jets and the missing transverse energy.

Forward calorimeter

The Forward Calorimeter (FCal) cover the very forward region of pseudorapidity $3.1 < |\eta| < 4.9$ making the calorimeter system achieve its good hermeticity and minimize the energy losses. It has an electromagnetic part that uses copper as absorber and two hadronic compartments with tungsten as passive material.

2.2.5 Muon spectrometer

The most external detector system is the muon spectrometer, a combination of toroidal superconducting magnets (Section 2.2.2) and precision chambers providing a measurement of the momentum of muons in $|\eta| < 2.7$ in addition to the measurement from the ID. It is also equipped with an independent trigger system used for the first event triggering stage (see Section 2.4.1) active in the pseudorapidity region $|\eta| < 2.4$.

Four sub-detectors compose the muon system: Monitored Drift-Tube (MDT) chambers, Cathode Strips Chambers (CSC), Resistive Plate Chambers (RPC) and Thin Gap Chambers (TGC). The layout changes in the barrel and end-cap regions, and is schematically shown in Figure 2.12(b): in the barrel region, chambers are arranged in three cylindrical layers around the beam axis, one layer being inside the magnet; in the end-caps these three layers are placed perpendicular to the beam axis.

Detection chambers

MDTs and CSCs are used to detect muons in the pseudorapidity regions $|\eta| < 2.0$ and $2.0 < |\eta| < 2.7$ respectively. MDTs are proportional chambers constituted by pressurised drift tubes made of aluminium with a diameter of 30 mm and lenght varying from 0.9 m to 6.2 m. The gas mixture in them is 93% argon and 7% carbon dioxide, the anode is a $50 \mu\text{m}$ tungsten-rhenium wire producing a radial electric field. Each chamber is composed by a group of six or eight tubes placed transverse to the beam axis. This number of tubes allows for a very good track reconstruction and high reduction of the fake tracks from random associations of background hits, providing a resolution on position of $80 \mu\text{m}$.

The CSCs are used at higher η to better cope with the higher particle flux. They are arranged in a system of two disks with eight chambers each. Each chamber contains four multiwire proportional chambers (the CSCs) with wires oriented in the radial direction, spaced by 2.5 mm and in the same gas mixture of argon and carbon dioxide as the MDTs.

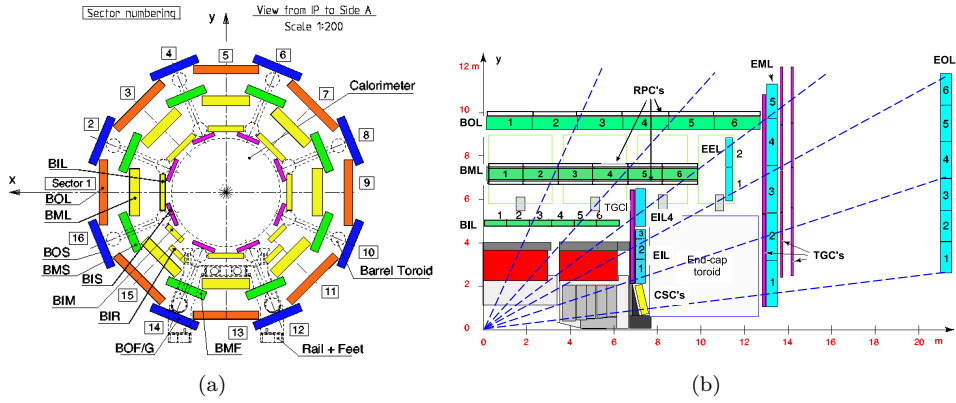


Figure 2.12: (a) Cross section of the barrel muon system. (b) Lateral section of the muon system. Barrel MDTs are shown in green, end-caps MDTs in light blue, CSC in yellow, TGCs in magenta, RPCs in white.

414 The cathode strips are oriented one perpendicularly to the anode wires (and gives the pre-
 415 cision coordinate) and the other parallel to the wires (and gives the transverse coordinate).
 416 The resolution provided by the interpolation between the charges induced on neighbouring
 417 cathode strips ranges between 50 and 70 μm .

418 Trigger chambers

419 For trigger purposes detectors with faster response than drift tubes are needed⁶. MDTs
 420 and CSCs are then coupled with special layers of trigger chambers: in the barrel region, the
 421 MDT's second layer is covered on both sides by RPCs, while MDT's third layer is covered
 422 by a RPC alternatively on the inner and outer side; in the endcaps, TGCs cover the inner
 423 side of MDT's first and third layers.

424 A RPC is a detector with a gas-gap between two resistive bakelite plates separated by
 425 2 mm and containing a gas mixture of $\text{C}_2\text{H}_2\text{F}_4$ (94.7%), $\text{Iso-C}_4\text{H}_{10}$ (5%) and SF_6 (0.3%).
 426 RPCs measure six points per coordinate for each particle, quickly collecting the avalanches
 427 with two orthogonal sets of pick-up strips that provides a position resolution of 1 cm in each
 428 plane and 1 ns time resolution, allowing for individual bunch crossing discrimination. Also
 429 RPCs provide the ϕ coordinate for the tracks in the final analysis, since MDTs only give
 430 the η coordinate.

431 TGCs are similar to CSCs, have 1.8 mm wire-to-wire separation and 1.4 mm wire-to-
 432 cathode separation. They use a highly quenching gas mixture of CO_2 55% and $\text{n-C}_5\text{H}_{12}$
 433 45% and provide a spatial resolution of about 1 mm and a time resolution of 5 ns.

434 2.3 Forward sub-detectors

435 ATLAS is equipped with some detectors in the forward regions to perform additional
 436 measurements or monitoring studies. In particular, the Minimum Bias Trigger Scintillators

⁶Drift-time in tubes with a diameter of $\mathcal{O} \sim 10$ mm can be of ~ 500 ns, too long with respect to the 25 ns spacing of the bunch crossings.

Figure 2.13: Schematic of a section of TileCal barrel and extended barrel modules, with the cells division. The parts labelled with “E” are the MBTS.

(MBTS), that are somehow embedded in the structure of TileCal extended barrel modules (see Figure 2.13) and share with it the readout electronics, as they are also read by wavelength-shifting fibers. The MBTS consist of 32 scintillator paddles assembled in two disks covering the pseudorapidity region $2.09 < |\eta| < 3.84$ and are used for trigger purposes to detect minimum bias activity during the first runs of the LHC.

MBTS are also used for relative luminosity measurements, but there are two detectors specifically built to determine the luminosity delivered to ATLAS: LUCID and ALFA. LUCID (Luminosity measurements using Cerenkov Integrating Detector) is made of 32 tubes surrounding the beam pipe 17 m far from the interaction point on both sides of ATLAS and measures the luminosity bunch by bunch. ALFA (Absolute Luminosity For ATLAS) is only activated during special runs, and consists of 8 scintillating fibers detectors placed at 240 m from the interaction point inside roman pots, above and below the beam pipe.

Another luminosity monitorer is the Zero-Degree Calorimeter, whose main purpose is to determine the centrality of heavy-ion collisions. Placed at 140 m from the interaction point on both sides of the beam axis, is made of quartz rods alternated with tungsten plates.

Finally, the Beam Condition Monitor (BCM) is made of two sets of diamond sensors located 184 cm close to the interaction point along the beam and 5.5 cm close along R . Its task is to detect beam losses, potentially harmful for ATLAS, and in that case to alert LHC in order to stop the accelerator.

2.4 Trigger system

It was already introduced at the beginning of this Chapter the issue faced by LHC experiments of dealing with a huge amounts of events at very high frequencies. We remind that considering the nominal LHC luminosity of $10^{34} \text{ cm}^{-2} \text{ s}^{-1}$ a rate of interactions of 40 MHz is expected! This poses serious technical difficulties as the maximum frequency at which data can be recorded is limited to 200 Hz considering the limited capacity for storage.

ATLAS developed a trigger system able to reduce by a factor of 10^6 the amount of data to be kept by selecting only interesting physics events. The system is divided in three levels characterized by increasing sophistication and diminishing speed. At the very first indeed we will need a really quick and simple criterium to reject uninteresting events. The reduced information can then be processed with somehow slower logic by the other two High Level Triggers (HLT). A drawing of the system is shown in Figure 2.14.

Most of the trigger chains used for physics are un-scaled in the sense that all the events passing the selection are kept, but there are also pre-scaled trigger chains that contain either too many events or events considered not physically interesting. These trigger chains are used for checks or calibration rather than physics analysis, and the prescaling value P means that of all the events that would have passed the trigger, $1/P$ were accepted.

With the term “trigger chain” we refer to the sequence of selections defining a certain

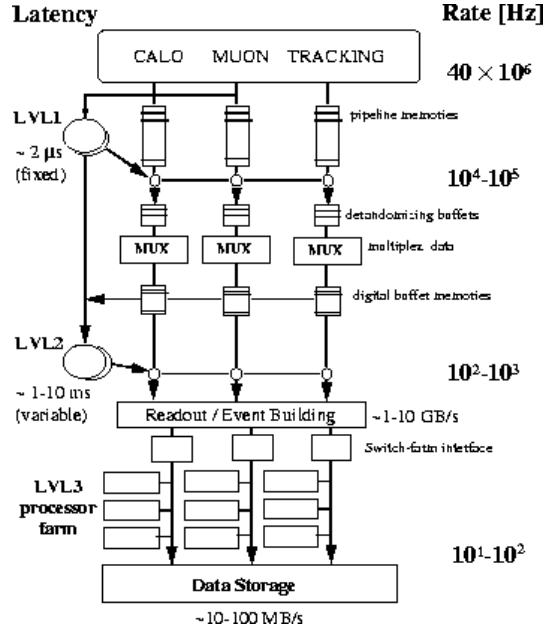


Figure 2.14: Schematic drawing of the three-level trigger system of ATLAS.

trigger object, with a naming convention like:

$$[\text{LEVEL}][\text{N}][\text{TYPE(S)}][\text{THRESHOLD}][\text{ISOLATION}][\text{QUALITY}],$$

where the components, from left to right, are: the trigger level used; the multiplicity of the type; the object candidate; the threshold applied to the transverse momentum or energy of the object candidate; the object isolation; the severity of the final algorithm requirements (this applies only to the Event Filter level).

Trigger chains define a *trigger menu*, where they are associated to their prescale value P , and which is chosen based on the physics program of the data taking period taking into account the LHC luminosity.

Defining the data taking period time unit as “Luminosity Block” (LB), typically a few minutes of data taking, information on beam conditions, detector performance and events passing any of the trigger chains of the trigger menu are stored to be then used in the analyses. All the LB occurring between the start and the end of a stable beam collision period compose a “run”. Runs are finally grouped in “Data Periods”, labelled with capital letters (“Period A”, “Period B”, *etc.*), when they pertain to the same general detector condition, machine configuration and trigger menu.

2.4.1 Level 1 trigger

The Level 1 trigger (L1) is completely based on the hardware of the detector, taking information from calorimeters, from the muon spectrometer trigger systems RPC and TGC (Section 2.2.5) and from the MBTS (Section 2.3) at 40 MHz (the frequency of the beam crossing) and reducing it to 75 kHz by choosing events with high transverse momentum or

high missing transverse energy.

Using dedicated fast front-end electronics (the typical decision time being less than $2\ \mu\text{s}$), calorimeter cells are analogically summed to build calorimetric towers which, if having an energy higher than a certain threshold, will activate a trigger chain.

These trigger chains will then be combined with the information from the muon spectrometer to form the so-called Region of Interest (RoI) that is passed to the next trigger level.

2.4.2 Level 2 trigger

Starting from the RoI, the Level 2 trigger (L2) will reduce the 75 kHz to 3.5 kHz of events with an average decision time of 40 ms. At this stage the information from the trackers is incorporated to the RoI to build candidate object (electrons, photons, muons) and better obtain its position and energy with simplified algorithms quick enough to respect the limit on the decision time.

2.4.3 Event filter

The last trigger, Level 3, is called Event Filter (EF) since at this point the physics objects are built using the same algorithms as the off-line reconstruction, with looser selections. With an execution time amounting to 4 s, the EF reduces the event rate to the goal value of 200 Hz. Events passing the EF are assigned to *streams* defined to separate the events into different datasets for different analysis interests, e.g. electron streams, muon streams, jet streams *etc.*

As an example, one of the trigger chains used in our analysis is `EF_mu24i_tight`: it selects events at the EF level with one muon with $p_T > 24\ \text{GeV}$ and some isolation requirement which passes the muon reconstruction algorithm cuts defined as “tight” (more on event reconstruction is reported in the dedicated Chapter 4).

2.5 Data Quality

The totality of p-p collisions recorded by ATLAS, which differs from the amount delivered by the LHC because of data-taking inefficiencies, is still not 100% usable by physics analyses. Indeed, every subdetector needs to perform some routine checks on the quality of the data they recorded in order to certify that its performance was conform to the expectations. So-called “Good Runs Lists” (GRL) are compiled stating for each LB what was “OK” and what not. The single analyses will then decide which GRL to use, based on their specific needs of the individual subsystems.

525 Monte Carlo simulation

526

527 3.1 Parton shower

528 3.2 Hadronization

529 3.3 Underlying-event

530 Underlying events are the product of the hadronic character of p-p hard interaction,
531 where the main collision process is accompanied by secondary parton interactions at low
532 transferred momentum (soft QCD) and are flavor- and color-connected to the hard scattering.
533 They are observed as jets of particles close to the direction of the beam and are in general
534 not separable from the event of interest. Their contribution can be studied with Monte
535 Carlo techniques tuned with data from *minimum bias* events, as perturbative theory does
536 not properly model low momentum QCD.

537 3.4 Generators

539 Event reconstruction

540

541 After having described the ATLAS detector in Chapter 2 and the procedure for Monte
 542 Carlo simulation of events in Chapter 3, we understand that what we deal with when we talk
 543 about “data” is raw digital signals from the detector, either the real one or the simulated
 544 one.

545 In the following Chapter we will explain how, starting from these outputs, objects are
 546 reconstructed to be used in physics analyses [17]. This process is what is called “offline event
 547 reconstruction” since it is not done in real time, due to the time required by the algorithms
 548 to perform their tasks.

549 In general we could describe the full procedure as subdivided into three main steps: a
 550 pre-reconstruction stage where the electronic signals are translated into measurements; a
 551 pattern-recognition step where the measurements are assembled into the building blocks of
 552 particles, e.g. tracks and energy clusters; a particle identification final leg where the full
 553 detector information elaborated is combined to match a candidate physics object (electrons,
 554 muons, jets and the missing transverse energy E_T^{miss}).

555 The expected signatures for the various particles in terms of interaction with the detector
 556 system are schematically shown in Figure 4.1.

557 4.1 ID Tracks

558 Particle trajectories (“tracks”) are used both to reconstruct the particle itself, giving the
 559 momentum measurement, and to identify the interaction vertices. The parameters describing
 560 a track are: q/p , the charge divided by the momentum; θ , or more used η , the angle with
 561 respect to the Z axis in the RZ plane measured from the perigee¹; ϕ_0 , the angle with respect
 562 to the X axis in the XY plane measured from the perigee; d_0 , the impact parameter, or
 563 perigee with respect to the Z axis in the XY plane; z_0 , Z component of the perigee. These
 564 parameters are shown in the double-view drawing of Figure 4.2.

565 In order to reconstruct the track, the first step is to retrieve the information from the
 566 ID hits, which are converted into three-dimensional space points. Then, the *inside-out*

¹The perigee is the point of the track closest to the origin.

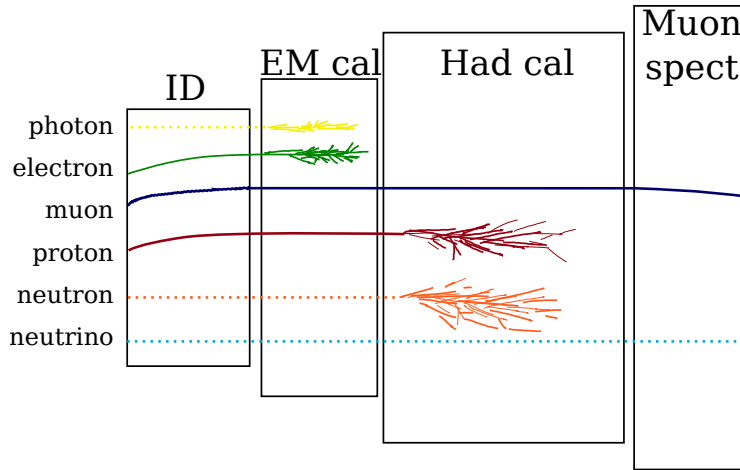


Figure 4.1: Drawing illustrating how particles are detected in the ATLAS sub-systems.

algorithm [18] is used, starting from a seed of three aligned hits in the pixel detector or in the SCT. From there, a path is formed along the seed directional information adding space points one by one. This is done by using a Kalman filter algorithm [19] which checks progressively the compatibility between the track (also progressively updated) and the new point. The five track parameters described before are also computed at this step. A cleaning procedure then rejects incomplete tracks or tracks sharing hits with others, or composed by false space points. The candidate tracks are extended into the TRT and re-fitted taking into account the effects from the interaction of the charged particle with the detector material.

A second algorithm, called *outside-in*, is applied in order to better reconstruct tracks from secondary charged particles. This algorithm does the opposite of the inside-out one, taking as seeds hits in the TRT (the ones not associated to any track candidate in by the inside-out reconstruction) and extrapolating back to the SCT and pixel detector.

4.2 Primary vertices

In general, a primary vertex (PV) is identified by the tracks associated to it. The reconstruction is performed via an iterative procedure [20] starting from a seed defined as the maximum in the distribution of the z_0 parameter of reconstructed tracks. After tracks are assigned to the PV with the aid of an iterative χ^2 fit, the ones that fall out of more than 7σ from the PV are used to seed another PV until no track is left without being assigned to a vertex (one track can be associated to more than one vertex).

A PV must have at least two associated tracks and its position must be consistent with the beam collision region in the XY plane. The hard-scatter PV is chosen as the one with the highest sum of squared transverse moments of the tracks. The other reconstructed PVs are identified with pile-up interactions. Another kind of vertices, not compatible with the requirement of coming from close to the proton collision spot, are the secondary vertices, originating from the decay of short-lived particles. These vertices are useful to identify B -hadrons and will be described in Section 4.6.2.

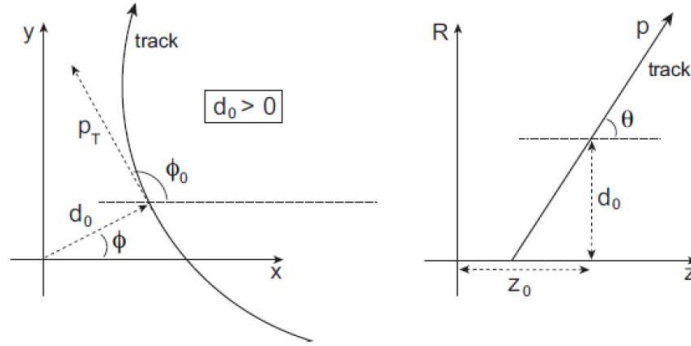


Figure 4.2: Schematic drawings of the parameters used for track reconstruction in the XY and RZ planes (left and right respectively) where the origin is the beam spot, i.e. where the protons collide and interact.

As can be expected, high pile-up environments deteriorate the performance of vertex reconstruction, as more fake tracks are introduced and nearby interaction might lead to the misreconstruction of distinct vertices as a single one [21].

4.3 Energy clusters

With the name “energy cluster” we generically refer to energy deposits in the calorimeter cells that are grouped together on the basis of some criteria [22]. In particular, we are interested in *topological clusters* and *electromagnetic towers*, used respectively for jets and electron/photon reconstruction.

Topological clusters, abbreviated as “topoclusters”, are built from neighboring calorimeter cells starting from a seed deposit with a signal (S , the cell measured energy) to noise (N , the RMS of the cell noise distribution) ratio higher than a certain threshold. Cells with $S/N \geq 4$ are taken as seeds, and starting from the one with the highest S/N all the neighboring cells with $S/N \geq 2$ are added to the topocluster. Topoclusters are treated as massless and their energy at the electromagnetic scale is the sum of the constituent cells. Their position and direction parameters are obtained from a weighted sum of the constituent cells’ pseudorapidity and azimuth angle based on the absolute value cell’s energy. Since energy measurement can be negative (due to noise fluctuations), clusters with negative energies are rejected.

Towers are built using the *sliding window* algorithm [23] starting from single energy deposits in the EM calorimeter middle layer of size $\Delta\eta \times \Delta\phi = 0.025 \times 0.025$. As schematically shown in Figure 4.3, a window of 3×5 cell units is defined, centered on the maximum of energy and finally expanded to optimize the cluster reconstruction, with a size that depends on the object (electron or photon) and the position in the detector (3×7 in regions with $|\eta| < 1.4$ and 5×5 elsewhere).

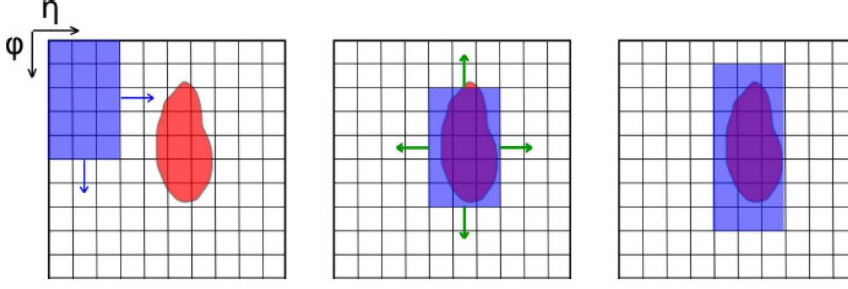


Figure 4.3: The three steps of the sliding window algorithm.

4.4 Electrons

Electrons [23] are reconstructed for pseudorapidities up to $|\eta| = 2.47$, where information from the ID is available, matching a track (see Section 4.1) with a cluster in the electromagnetic calorimeter reconstructed with the sliding window algorithm (see Section 4.3). In order to account for bremsstrahlung losses the matching is done within a region of dimension $\Delta\eta \times \Delta\phi = 0.05 \times 0.10$ and if more candidate tracks are matched, of all the ones with hits in the silicon detectors the track with the smallest ΔR with respect to the energy cluster is chosen. In addition, the track momentum has to be compatible with the cluster energy, which is calibrated to the electromagnetic scale derived from Monte Carlo based corrections (to account for dead material losses), test-beam studies and calibration from $Z \rightarrow ee$ events [24, ?].

In general, electron can be distinguished from hadrons thanks to various characteristics of their shower development: electrons deposit the most of their energy in the second layer of the EM calorimeter; the width of their shower is narrower; they have smaller hadronic leakage²; the E/p variable (ration of cluster energy and track momentum) is higher.

Some difficulties arise when dealing with π^0 and η particles, which decay into two γ s that produce two close showers reconstructed as a single one in the second layer of the EM calorimeter, and in general with jets faking electrons from, e.g. QCD processes. There are then six different electron definitions to help separate real electrons from fake ones, described in the following ordered from the looser requirements to the tightest. Performance studies on electron reconstruction and identification where done using 2010 data and Monte Carlo $Z \rightarrow ee$ and $W \rightarrow e\nu$ events [23] (see Figure 4.4).

Loose electrons lie in the pseudorapidity region $|\eta| < 2.47$ and have low hadronic leakage and requirements on the variables defining the shower shape. The identification efficiency is high but the jet rejection is low (about 500).

Loose++ electrons are **loose** electrons whose track has at least one hit in the pixel detector and at least 7 hits in the combined silicon detectors and the $|\eta_{\text{firstEM}}|$ distance between the track extrapolated to the first EM layer and the matched cluster is lower than 0.015. The identification efficiency is similar to the loose one but the rejection is ten times

²The hadronic leakage is the ratio of the transverse energy reconstructed in the first layer of the hadronic calorimeter to the total transverse energy reconstructed in the EM calorimeter.

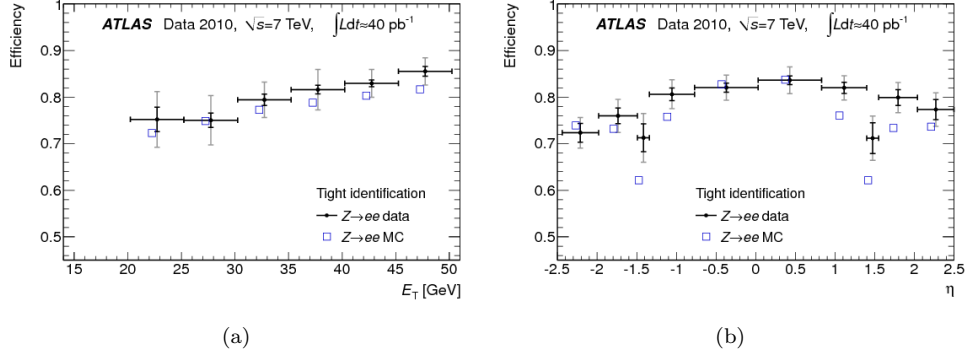


Figure 4.4: Tight electron identification efficiencies measured from $Z \rightarrow ee$ events and predicted by MC as a function (left) of E_T (integrated over $|\eta| < 2.47$ excluding the transition region $1.37 < |\eta| < 1.52$ and (right) of η and integrated over $20 < E_T < 50$ GeV. [23]

higher.

Medium electrons are `loose++` electrons where additional requirements on shower shape are made as well as on their tracks: $|d_0| < 5$ mm and $|\eta_{\text{firstEM}}| < 0.01$. The efficiency drops to 88% and the rejection is higher than the previous.

Medium++ electrons are `medium` electrons whose track has at least one hit in the first pixel detector layer, a requirement that allows to reject electrons from photon conversion. Charged hadrons contamination is reduced by discarding candidates whose track has a low fraction of high-threshold TRT hits. In addition, $|\eta_{\text{firstEM}}| < 0.005$ and stricter cuts are applied to shower shaper of clusters in $|\eta| < 2.01$. The efficiency is about 85% and rejection is about 50×10^3 .

Tight electrons are `medium++` electrons with additional requirements on the distance between the track and the matched cluster ($|\Delta\phi| < 0.02$, $|\Delta\eta| < 0.005$) and on the E/p variable. Stricter cuts are imposed on the fraction of high-threshold TRT hits and on the impact parameter ($|d_0| < 1$ mm). The efficiency drops to 75% and the rejection is higher than the previous one.

Tight++ electrons are `tight` electrons with asymmetric $\Delta\phi$ cuts, which give both better efficiency and rejection.

4.4.1 Additional requirement and corrections for analyses

For our analyses [25], electrons in the transition region $1.37 < |\eta_{\text{cluster}}| < 1.52$ with inactive material are excluded. Electrons are required to satisfy `tight++` criteria and to have $E_T = E_{\text{cluster}} / \cosh \eta_{\text{track}} > 25$ GeV and $z_0 < 2$ mm. In addition, to suppress further the QCD multijet background, isolation cuts are imposed both as calorimeter (using the energy in a cone of size $\Delta R < 0.2$, `EtCone20`) and track isolation (using the scalar sum of p_T s from tracks within a cone of $\Delta R < 0.3$, `PtCone30`). The `EtCone20` and `PtCone30` isolation cuts are chosen to give 90% efficiency. In addition, jets (see Section 4.6) within $\Delta R = 0.2$ of the selected electron are discarded, and if an additional jet with $p_T > 25$ GeV and $|JVF| > 0.5$ is found within $\Delta R = 0.4$, then the electron is rejected. The electron is

673 matched to the single electron trigger `EF_e24vhi_medium1` combined with a logical OR to the
 674 `EF_e60_medium1` trigger, which recovers some efficiency loss at $E_T > 80$ GeV.

The efficiency in selecting electrons can be factorized as:

$$\varepsilon = \varepsilon_{\text{reco}} \cdot \varepsilon_{\text{tight}++} \cdot \varepsilon_{\text{isolation}} \cdot \varepsilon_{\text{trigger}} \quad (4.1)$$

675 where the various components represent respectively: the efficiency in reconstructing the
 676 electron in terms of track-cluster match, track quality and hadronic leakage; the efficiency
 677 for the `tight++` identification criteria; the efficiency for the isolation cuts; the efficiency from
 678 trigger selection. Scale factors are derived in bins of (η, E_T) , and the trigger scale factors
 679 are separated into four data-taking periods (A-B3, B4-D3 without C1-C5, C1-C5 and D4+).
 680 The efficiency scale factors are applied as weights to Monte Carlo events.

681 The electron energies in data are corrected using scale factors $\alpha(\eta)$ derived from data-
 682 to-simulation comparison in $Z \rightarrow ee$ events in order to match the Z boson mass peak.

683 4.5 Muons

684 As suggested in Figure 4.1, muons interact with all of ATLAS sub-detectors, even though
 685 they act as minimum ionizing particles (mip) for the calorimeters and hence will deposit only
 686 a very small fraction of their energy in the material. Their track instead is precisely measured
 687 both in the ID and in the muon spectrometer (MS). Based on how we decide to combine the
 688 various information, we can list the following types of reconstructed muons: **standalone**
 689 muons take the MS track and extrapolate it back to the interaction point; **combined** muons
 690 match the MS track with the tracks from the ID; **segment tagged** muons extrapolate ID
 691 tracks to the spectrometer and match the result with MS segments; **calorimeter tagged**
 692 muons extrapolate ID tracks to the calorimeters and match the result with energy deposits.

693 We will only consider **combined** muons, reconstructed using an algorithm called `Muid` [26]
 694 and whose pseudorapidity is limited to $|\eta| < 2.5$ by the ID acceptance. Starting from
 695 $\Delta\eta \times \Delta\phi = 0.4 \times 0.4$ regions where interesting activity has been triggered, track segments
 696 are searched for in the RPC and TGC and combined into a single track by means of a
 697 least-square fitting method. These track candidates are hence extrapolated back to the
 698 interaction point and their momentum corrected for the mip energy loss in the calorimeter
 699 material.

700 At this points a χ^2 test (checking the difference between the extrapolated track coor-
 701 dinates weighted with combined covariance matrix) on the matching of the candidate MS
 702 track and the tracks reconstructed in the ID is performed to obtain the final muon candidate
 703 track. Only ID tracks that satisfy some quality requirements are considered for the match-
 704 ing: they need to have at least two pixel hits, of which at least one in the first layer; at least
 705 two pixel hits plus number of crossed dead pixel sensors; at least six SCT hits plus number
 706 of crossed dead SCT sensors; maximum two pixel or SCT holes³; defining the number of
 707 TRT outliers⁴ and the number of TRT hits as N_{TRT_o} and N_{TRT_h} respectively, $N_{\text{TRT}_h} > 5$

³A “hole” in the silicon detectors is a region where the module did not perform as expected even though the surrounding ones did.

⁴“Outlier” is an hit that is deviated from the track path.

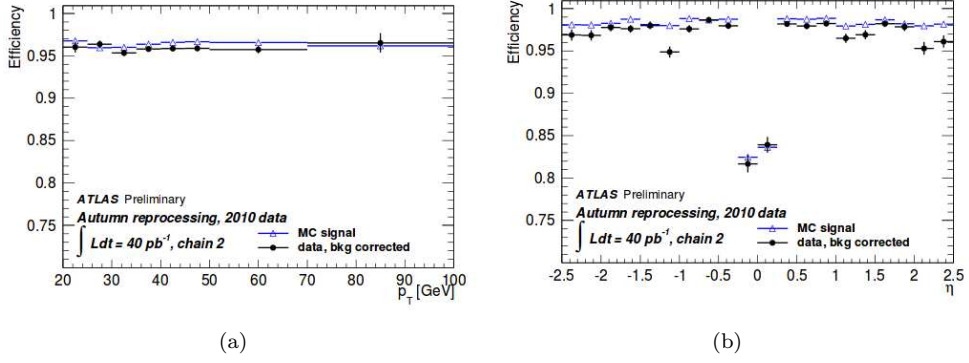


Figure 4.5: Combined muon reconstruction efficiencies using the Muid algorithm measured from $Z \rightarrow \mu\mu$ events and predicted by MC as a function (left) of p_T and (right) of η . [26]

and $N_{\text{TRT}_o}/N_{\text{TRT}_h} < 0.9$ for $|\eta| < 1.9$, $N_{\text{TRT}_o}/N_{\text{TRT}_h} < 0.9$ if $N_{\text{TRT}_h} > 5$ for $|\eta| \geq 1.9$. In case no matching is found, no muons are reconstructed, while if more candidates arise, the one giving the best χ^2 is chosen. The momentum is computed as a weighted average of ID and MS measurements.

Performance studies on muon reconstruction and identification were done using 2010 data and Monte Carlo $Z \rightarrow \mu\mu$ events [26] (see Figure 4.5).

4.5.1 Additional requirement and corrections for analyses

Combined muons are used in our analyses [25] with an additional cut on the longitudinal impact parameter $|z_0| < 2$ mm to ensure the track comes from the hard-scattering primary vertex. A requirement on the muon momentum of $p_T > 25$ is used to obtain 90% efficiency from the chosen single muon trigger, which is the logical OR combination of the triggers EF_mu24i_tight and EF_mu36_tight. The EF_mu24i_tight trigger includes an isolation requirement for which the p_T sum of the tracks in a cone of size $\Delta R = 0.2$ around the muon has to be less than the 12% of the muon transverse momentum. Muons overlapping with any jet (see Section 4.6) with $p_T > 25$ GeV and $|JVF| > 0.5$ within a $\Delta R < 0.4$ cone are rejected.

In addition to the previous isolation requirements, a “mini-isolation” is defined [25] to better deal with the high pile-up present in $\sqrt{s} = 8$ TeV collision events. The mini-isolation is defined as

$$I_{mini}^l = \sum_{tracks} p_T^{track} / p_T^l \quad (4.2)$$

where p_T^l is the lepton transverse momentum and the summation runs over all tracks found in a cone whose radius varies as a function of the muon momentum as:

$$\Delta R(l, track) = \frac{10 \text{ GeV}}{p_T^l}. \quad (4.3)$$

The tracks also have to satisfy: $p_T^{track} > 1$ GeV; $d_0 < 10$ mm; $z_0 \sin \theta_{track} < 10$ mm; at least four hits or dead sensors crossed in the silicon detectors. The cut on the mini-

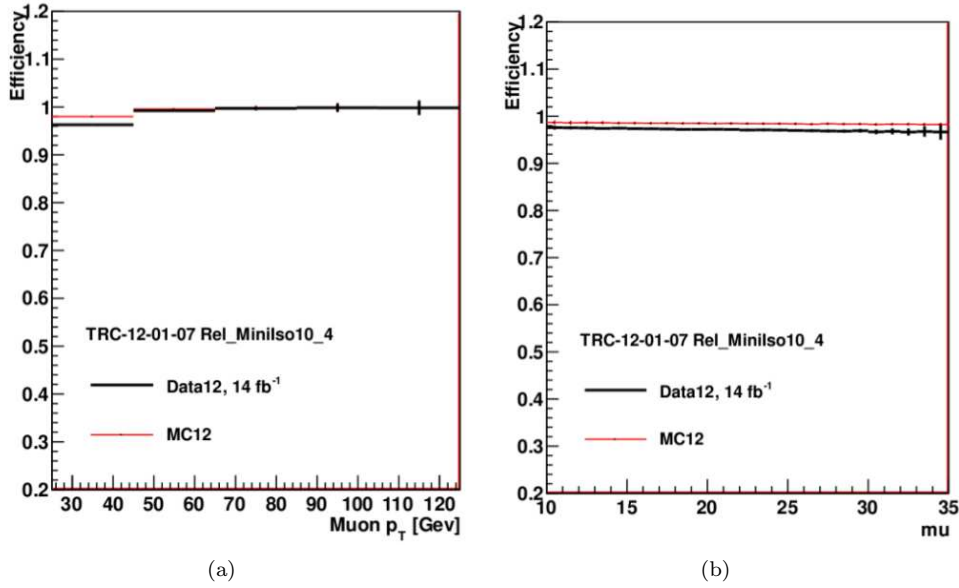


Figure 4.6: Efficiency of the mini-isolation as a function of the muon momentum (left) and of the average number of bunch crossings $\langle \mu \rangle$ (right) [25].

isolation variable is chosen as $I_{mini}^l < 0.05$. The performance of the mini-isolation is shown in Figure 4.6.

As is done for electrons, a set of corrections are applied to correct for minor discrepancies between Monte Carlo simulation and data events. The scale factors to compensate reconstruction, isolation and trigger inefficiencies are derived from tag-and-probe measurements and applied to Monte Carlo events. In addition, the muon momentum in simulated events is smeared to obtain agreement between the momentum resolutions in Monte Carlo and data.

4.6 Jets

With the name “jet” we generically refer to the object formed as a consequence of parton hadronization from a spray (or *jet*) of particles. These particles will leave signals both as tracks in the ID and as energy deposits in the calorimeters and two type of jets can then be defined using either the former or the latter information: track jets and calorimeter jets. In the following, we will only deal with calorimeter jets.

In order to interpret the detector information, first topoclusters are formed from the calorimeter cells signals, as explained in Section 4.3. Then, different algorithms were developed to associate topoclusters into a jet. Because of the need for a stable and precise performance over the QCD processes from p-p collisions, a set of requirements has been defined for the algorithms to be valid [27].

First of all, the splitting of one particle into two collinear particles must not change the result of the algorithm reconstruction, as well as the presence of additional soft emission. The importance of Infrared and Collinear (IRC) safety is evident considering e.g. that a hard parton, as part of the fragmentation process, will undergo many collinear splittings,

and that QCD events always include emission of some soft particles, perturbatively or not. In addition, we want the algorithm result to be invariant under Lorentz boost along the beam direction, to be as insensitive as possible to detector effects like noise or resolution, and to be light in terms of computing resource usage.

A set of jet algorithm that satisfy these requirements are the sequential recombination algorithms [28, 29, 30], which combine topoclusters into jets using as criteria a distance parameter defined as:

$$d_{ij} = \min(p_{T_i}^{2p}, p_{T_j}^{2p}) \frac{\Delta R_{ij}^2}{R^2}, \quad (4.4)$$

$$d_i = p_{T_i}^{2p}, \quad (4.5)$$

where p_{T_i} is the transverse momentum of topocluster i , $\Delta R_{ij} = \sqrt{\Delta\eta^2 + \Delta\phi^2}$ the distance between constituents i and j , R a parameter of the algorithm that approximately controls the size of the jet, p the parameter that defines the type of algorithm as:

$$\begin{aligned} p = 1 & : k_t \text{ algorithm;} \\ p = 0 & : \text{Cambridge/Aachen algorithm;} \\ p = -1 & : \text{anti-}k_t \text{ algorithm.} \end{aligned} \quad (4.6)$$

The algorithms compute d_{ij} , the distance between the two topocluster inputs i and j , and d_i , the distance between the input i and the beam axis in the momentum space. By computing the minimum of the two distances the choice made is to combine i and j into a new input if $d_{ij} < d_i$, or take i as a jet candidate and remove it from the input list if $d_i < d_{ij}$. The cluster combination is done by summing the four-momentum of each input. The distances are recalculated with the updated list of input objects and the process repeated until no further cluster is left.

The anti- k_t algorithm is chosen by most of analyses in ATLAS as it is particularly performant against pile-up, since it starts summing up constituents with higher momentum, and produces jets with a conical structure (see Figure 4.7(a)).

4.6.1 Additional requirement and corrections for analyses

For our analyses [25] jets are reconstructed using the anti- k_t algorithm with a radius parameter $R = 0.4$ (from which the algorithm is often referred to as anti- k_{t4}) using calorimeter energy deposits corrected for effects of non-compensation⁵, dead detector material and out-of-cluster leakage. Other effects affecting jet energy are low momentum particles that are deflected by the magnetic field and energy losses in topocluster formation and jet reconstruction [31].

The initial energy is reconstructed at the electromagnetic (EM) scale as the calorimeter signals arise from electromagnetic interaction of particles with matter. The energy calibration to EM scale was derived during test-beam runs using electron beams, validated with muons from both test-beam and cosmic-rays runs and corrected using simulated $Z \rightarrow ee$ events.

⁵The energy response to hadrons is lower than the response to electrons of the same energy due to the presence of invisible processes.

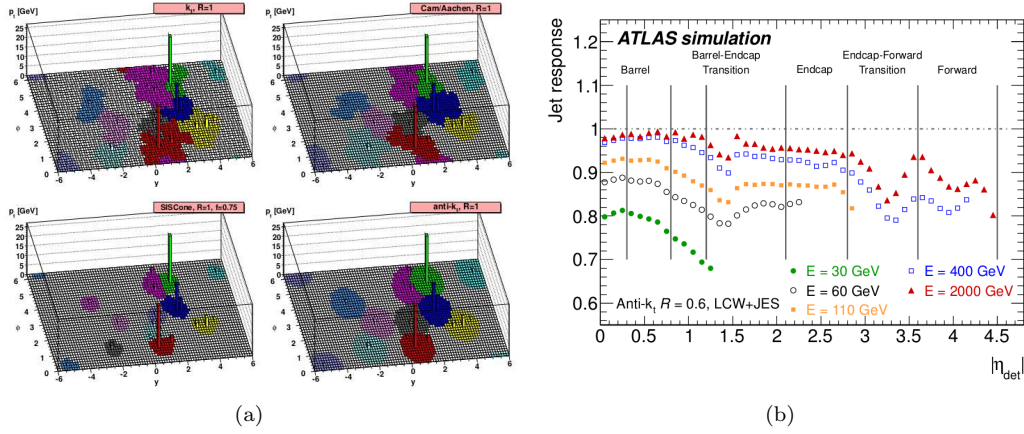


Figure 4.7: Left: The same input produces different results in terms of jet reconstruction using various jet algorithms [27]. Right: Average jet energy response from simulated events at the LCW scale for various calibrated energies (E) as a function of pseudo-rapidity. The inverse of the response shown in each bin is equal to the average jet energy scale correction [31].

Of the several energy calibration schemes derived in ATLAS, we will be using the Local Cluster Weighting (LCW) calibration [32, 33]. This scheme exploits properties of the topoclusters shapes to classify the clusters as “mainly electromagnetic” or “mainly hadronic” and then derives the calibration from Monte Carlo simulation of charged and neutral pion events. The calibration corrections are applied before the jet reconstruction algorithm is operated, and after the jet is formed a final correction is applied to ensure linearity in response.

In our analyses we consider only jets with $p_T > 25$ GeV and $|\eta| < 2.5$. Furthermore, a variable called “jet vertex fraction” (JVF) is defined as the fraction of the sum of p_T of tracks with $p_T > 1$ GeV associated with the jet that comes from tracks originating from the primary vertex. By requiring $JVF > 0.5$ we avoid selecting jets from in-time pile-up events.

To avoid double counting of energy deposits from electrons as jets, if jets are found within ΔR of 0.2 of the selected electron, the jet closest to the lepton is removed and then electrons that lie within $\Delta R < 0.4$ of the remaining jets are discarded.

4.6.2 b -tagging

When a bottom quark is produced in an events, it hadronizes into a B hadron, which has a lifetime of the order of 10^{-12} s and hence can travel about 3 mm before decaying. The result is a displaced secondary vertex that, if correctly reconstructed, can allow for the identification of the bottom quark. Since this capacity relies on track reconstruction from the ID, its applicability is limited by the ID acceptance to the pseudorapidity region $|\eta| < 2.5$.

This technique is called b -tagging [34] and is widely used in ATLAS analyses with top quarks. There are three types of algorithms, and they can be combined to obtain better performance. In general they define a weight corresponding to the probability for the jet

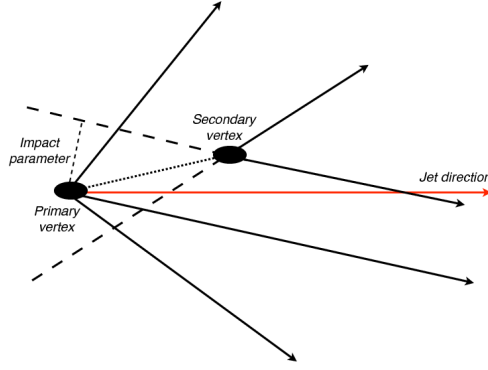


Figure 4.8: Simple schematic of the displaced secondary vertex.

799 to be tagged, and a working point is chosen as the threshold for this weight to discriminate
 800 between b - and not- b -jets by finding a good compromise between a good efficiency (the
 801 ratio between tagged b -jets and true b -jets) and a high light-jet rejection (the inverse of the
 802 number of light-jets misidentified as b -jets).

803 Algorithms like IP1D, IP2D and IP3D are based on information from impact parameters
 804 of the tracks contained in the jet, z_0/σ_{z_0} , d_0/σ_{d_0} and a combination of the two respectively.
 805 A likelihood is computed to obtain the b -tag weights.

806 Other algorithms reconstruct the secondary vertex from the B hadron decay, allowing
 807 for a better discrimination between b -jets and light jets. The SV1 algorithm uses the number
 808 of track pairs in the secondary vertex, their total invariant mass and the ratio of the sum
 809 of the energies of tracks from the secondary vertex to the one of the total tracks of the jet
 810 to compute likelihood ratios the logarithm of which are then summed to obtain the b -tag
 811 weights.

812 Finally, the JetFitter algorithm uses the full decay chain reconstruction of b and c
 813 hadrons by fitting it with a Kalman filter to determine a common path between the primary
 814 vertex and the vertices from the b and c hadrons inside the jet. The likelihood is computed
 815 with the flight length significances of the vertices and the variables from the SV1 algorithm.

816 The algorithm employed in our analyses is called MV1 and uses a neural network to
 817 combine information from the JetFitter, IP3D and SV1 algorithms. The working point
 818 corresponding to 70% efficiency, ~ 130 light-jet rejection and a charm-jet rejection of 5 is
 819 chosen (see Figure 4.9).

820 The tagging efficiencies in Monte Carlo are corrected for b and c flavours with the ap-
 821 propriate $\epsilon_{data}/\epsilon_{MC}$ scale factors, determined in bins of jet p_T and η .

822 Tag Rate Function method

823 When requiring ≥ 1 b -tagged jet the available Monte Carlo statistics is significantly re-
 824 duced for some particular background processes, leading to large fluctuations in the resulting
 825 distributions.

826 To overcome this problem the Tag Rate Function (TRF) method is introduced. Here,

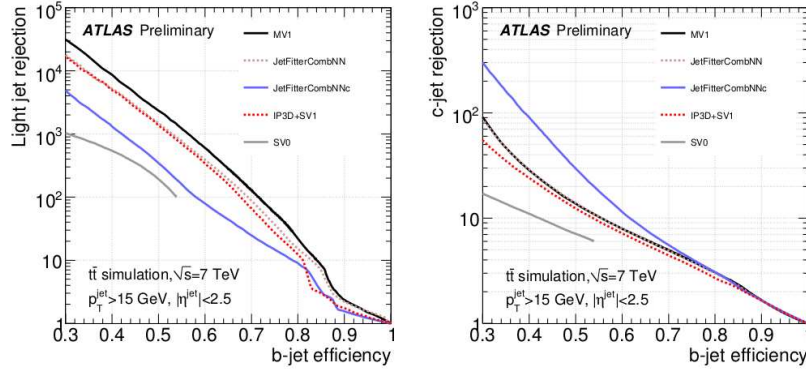


Figure 4.9: Light- (left) and c -jet (right) rejection as a function of the b -jet tagging efficiency for different tagging algorithms. These values refer to jets with $p_T > 15$ GeV and $|\eta| < 2.5$ in simulated $t\bar{t}$ events [35].

no event is rejected based on its b -tagging count, but instead all the events are kept and weighted according to the probability of the given event to contain the desired number of b -jets. The event weight is computed based on the kinematics and flavour of the jets found in each event and using the tagging efficiency, which is a function of η , p_T and true jet flavour.

Given a jet with η , p_T and flavour f , its tagging probability can be noted as:

$$\varepsilon(f, |\eta|, p_T)$$

For a given event with N jets, its probability of containing exactly one b -tag jet can be computed as:

$$P_{=1} = \sum_{i=1}^N \left(\varepsilon_i \prod_{i \neq j} (1 - \varepsilon_j) \right)$$

In the same way, it can be used to compute the probability for inclusive b -tag selections:

$$P_{=0} = \prod_{i=1}^N (1 - \varepsilon_i)$$

$$P_{\geq 1} = 1 - P_{=0}$$

Since this method relies on the correctness of the tagging efficiency, closure tests have been performed to check calibration of the tagging efficiency in Monte Carlo samples. These studies show that the efficiency parametrization officially provided [25] is not as accurate as expected, and therefore new efficiency maps were obtained. With correct calibrations the average of the histogram of $1/\varepsilon$ vs η , p_T and true jet flavour should be flat and with mean equal to one. Figure 4.10 shows these variables using the official and the new maps. It is clear that some regions of the light flavor map show high departure from closure, hence the new efficiency map will be used for the probability computations in the TRF method.

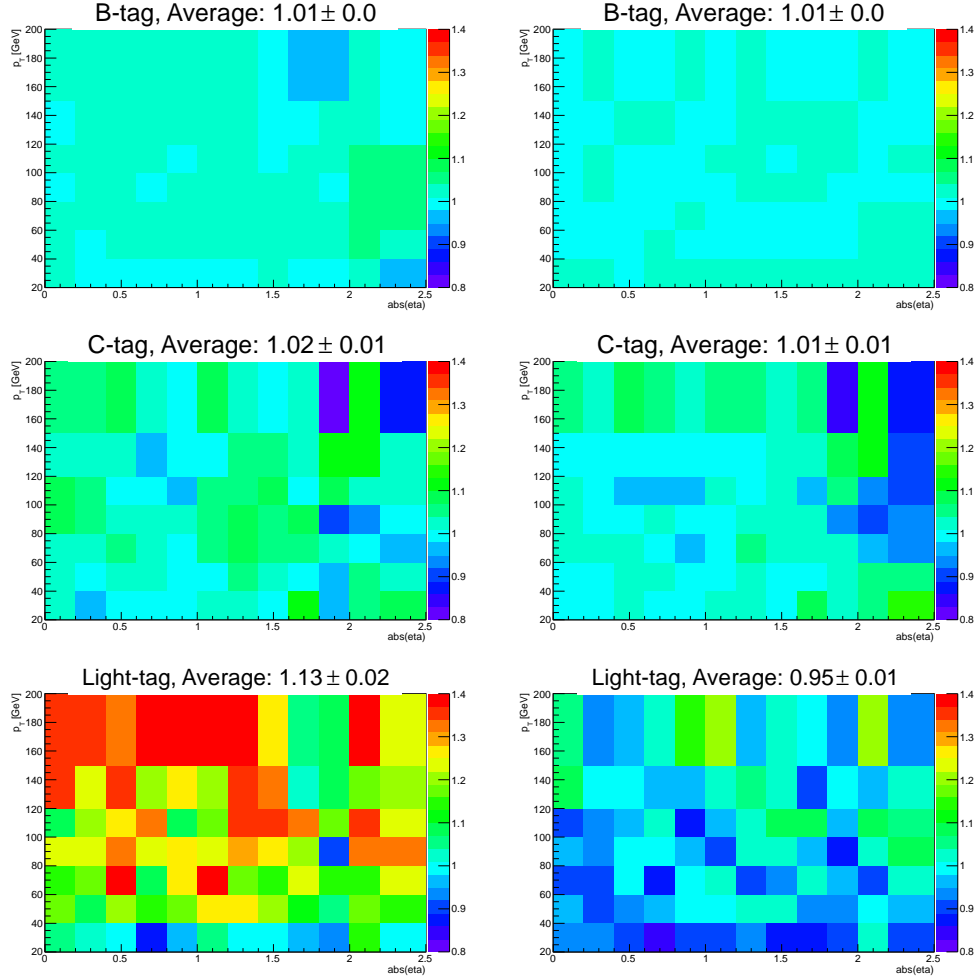


Figure 4.10: Results of the closure test using efficiency from the official calibration file (left column) and the private efficiency map (right column). The test is split in the different jet flavours: b jets (top), c jets (middle) and light jets (bottom).

4.7 Missing Transverse Energy

To estimate the momentum of invisible particles in the event, i.e. neutrinos and, eventually, new particles, the missing transverse energy E_T^{miss} [36] is defined [25] to balance the total transverse momentum of the event. Indeed, while the longitudinal energy of the interacting partons is unknown, as they carry an unpredictable fraction of the total proton momentum, its transverse component is, initially, zero. Possible sources of fake contributions to the E_T^{miss} are detector coverage, dead or noisy regions and finite detector resolution.

The E_T^{miss} is computed by first matching each calorimeter energy deposit is with a high- p_T object, in the following order: electrons, photons, jets and muons. These are respectively the RefEle, RefGamma, RefJet, RefMuon terms, whether the low- p_T jets are grouped into the SoftJet term. Then, the energies of these objects are corrected accordingly to the respective calibration constants. The calorimeter clusters that did not get associated with any high- p_T object are calibrated for energy losses in dead material regions and for the different response to the electromagnetic and hadronic components of particle showers and added as the CellOut term. Finally the E_T^{miss} is computed as:

$$\begin{aligned} E_{x,y}^{\text{miss}} &= E_{x,y}^{\text{RefEle}} + E_{x,y}^{\text{RefGamma}} + E_{x,y}^{\text{RefJet}} + E_{x,y}^{\text{RefMuon}} + E_{x,y}^{\text{SoftJet}} + E_{x,y}^{\text{CellOut}} \\ E_T^{\text{miss}} &= \sqrt{(E_x^{\text{miss}})^2 + (E_y^{\text{miss}})^2} \end{aligned} \quad (4.7)$$

848 Searches for vector-like top partner 849 pairs in the single lepton channel

850

851

852 In the following Chapter we will describe two searches for vector-like top partners $T\bar{T}$
853 pairs performed in the single lepton¹ channel. These analyses are optimized for different
854 final states and are thus complementary. The first search focuses on decay channels with
855 high BR to Wb and is performed using the full dataset of p-p collisions at the center of mass
856 energy of $\sqrt{s}=8$ TeV collected during 2012 at the ATLAS detector, consisting in 20.34 fb^{-1} ,
857 while the preliminary search for vector-like top partners with high BR to Ht uses a partial
858 dataset of the same data, amounting to 14.3 fb^{-1} .

859 The Chapter is organized as follows: first Section 5.2 introduces the common event pre-
860 selection for data and few general concepts in the analyses design; Section 5.3.1 presents the
861 Monte Carlo samples used in the searches, which are in general common to both analyses
862 with only few exceptions that are reported; Section 5.3.2 describes how the multi-jet back-
863 ground from QCD events is obtained. Finally, the two analyses are detailed in Section ?? and
864 Section ??, which illustrate the event selection criteria, the background modeling estimation,
865 the systematics affecting the analysis, the statistical treatment and the results.

866 5.1 General strategy for $T\bar{T}$ pairs searches

867 5.2 Data sample and common event preselection

868 The data from p-p collision events recorded at the ATLAS experiment during 2012
869 at a center of mass energy of $\sqrt{s} = 8$ TeV are considered. Physics object definitions were
870 previously discussed in Section ?. Events collected during stable beam periods are required
871 to pass data quality requirements and single lepton trigger selection. In order to maximize

¹From now on, with the word “lepton” we will mean only either electron or muon, assumed to come from the leptonic decay of a W boson with its associated neutrino, which is considered to be the only particle contributing to the transverse missing energy E_T^{miss} .

	Wb	Ht	Zt
Wb	4 (2)	6 (4)	6 (2/4)
Ht	6 (4)	8 (6)	max: 8 (4/6) min: 6 (2)
Zt	6 (2/4)	max: 8 (4/6) min: 6 (2)	max: 8 (2/6) min: 6 (2/4)

Table 5.1: Jets (b -jets) multiplicities in the various possible final states. Z boson decays 55% hadronically, 15% of the times into $b\bar{b}$, therefore the min/max number of b -jets is reported. Highlighted are the channels that after the orthogonality cut will contribute to the $T\bar{T} \rightarrow Wb+X$ analysis.

trigger efficiency, different transverse momentum threshold triggers are combined through a logical OR, with the lower p_T ones including isolation requirements that result in inefficiencies for high p_T lepton candidates, recovered with the use of the higher threshold triggers. The electron triggers have p_T thresholds of 24 and 60GeV, the muon ones of 24 and 36GeV.

After passing trigger requirements, events with more than one lepton are discarded. In addition, the only lepton of the event has to match within $\Delta R < 0.15$ the triggered one. As basic preselection, four jets satisfying the conditions described in Section 4.6 are required, at least one of them being tagged as a b -jet.

In order to suppress the multi-jet background from QCD processes, combined cuts on the E_T^{miss} and on the transverse mass of the leptonically decaying W boson m_T^2 are defined: $E_T^{\text{miss}} > 20 \text{ GeV}$ and $E_T^{\text{miss}} + m_T > 60 \text{ GeV}$.

At this point, a simple consideration about the typical expected jet (and b -jet) multiplicity is made so as to define an orthogonality cut between the two analyses. Table 5.1 shows the number of jets (b -jets) per decay channel combinations of $T\bar{T}$ pairs, in the case of single lepton selection with at least four jets (i.e. one W boson will always decay into lepton and neutrino, and Z boson decay to neutrinos is excluded in the $WbZt$ channel) and assuming that the Higgs boson decays to a bottom quark-antiquark pair. To avoid overlap between selected events from the two analyses, in the $T\bar{T} \rightarrow Wb + X$ analysis events with ≥ 6 jets and ≥ 3 b -jets are rejected³.

5.3 Background and signal modeling

The main background for both analyses is $t\bar{t}$ production with jets ($t\bar{t}$ +jets in the following) and different choices for the generator are made in the analyses because of the specific needs of having well modeled regions. In the case of the $t\bar{t}$ +jets background prediction for the $T\bar{T} \rightarrow Ht + X$ analysis further corrections to match the data are applied, due to a mis-modeling in the heavy- and light-flavour content of the simulated sample (see Section 7.2).

² $m_T = \sqrt{2p_T^\ell E_T^{\text{miss}}(1 - \cos \Delta\phi)}$, with p_T^ℓ being the transverse momentum (energy) of the muon (electron) and $\Delta\phi$ the azimuthal angle separation between the lepton and the direction of the missing transverse momentum.

³As will be explained later in Section 7.2, another orthogonality cut will be applied in the low b -jet multiplicity channel of the $T\bar{T} \rightarrow Ht + X$ analysis.

W boson production in association with jets (W +jets in the following) and multi-jet events from QCD processed also contributes, the latter sneaking into the event selection via the misidentification of a jet or a photon as an electron or the presence of a non-prompt lepton from, e.g., semileptonic b - or c -hadron decay. Other background smaller components are single top quark, Z +jets, diboson (WW, WZ, ZZ), and $t\bar{t}$ production associated with a vector or Higgs boson.

All event generators using HERWIG [?] are also interfaced to JIMMY v4.31 [?] to simulate the underlying event. With the exception of the signal samples, all simulated samples utilise PHOTOS 2.15 [?] to model photon radiation and TAUOLA 1.20 [?] to model τ decays.

All simulated samples include multiple p-p interactions and go through the GEANT4 [?] detector geometry and response simulation [?] with the exception of the signal samples, for which a fast simulation of the calorimeter response is used.

All simulated samples are then processed through the same reconstruction software as the data and are reweighted to match the instantaneous luminosity profile in data.

5.3.1 Monte Carlo simulated samples

$t\bar{t}$ MC@NLO

Simulated samples of $t\bar{t}$ pair production in association with jets ($t\bar{t}$ +jets or simply $t\bar{t}$ in the following) are generated with MC@NLO v4.01 [?, ?, ?] using the CT10 set of parton distribution functions (PDFs) [?], with the parton-shower and fragmentation steps being performed by HERWIG v6.520 [?]. The top quark mass is assumed to be equal to 172.5 GeV and the samples are normalized to approximate next-to-next-to-leading-order (NNLO) theoretical cross section [?]; the cross section used has been computed with HATHOR 1.2 [?] using the MSTW2008 NNLO PDF set [?] and is $\sigma_{t\bar{t}} = 238_{-24}^{+22}$ pb, where the total uncertainty results from the sum in quadrature of the scale and PDF+ α_S uncertainties according to the MSTW prescription [?]. This is the $t\bar{t}$ used in the $T\bar{T} \rightarrow Wb + X$ analysis.

$t\bar{t}$ Alpgen

Simulated samples of $t\bar{t}$ +jets are generated using the ALPGEN v2.13 [?] leading-order (LO) generator and the CTEQ6L1 PDF set [?], with parton shower and fragmentation modelled through HERWIG v6.520 [?].

A parton-jet matching scheme called “MLM matching” [?] is used in order to avoid double-counting of partonic configurations eventually generated both at the matrix-element calculation level and at the parton-shower evolution step.

Separate samples are generated for $t\bar{t}$ +light jets ($t\bar{t}$ +light or $t\bar{t}$ +LF in the following, from “light flavour”) with up to three additional light partons (u, d, s quarks or gluons), and for $t\bar{t}$ +heavy-flavour jets ($t\bar{t}$ +HF in the following), including $t\bar{t}b\bar{b}$ and $t\bar{t}c\bar{c}$. An algorithm based on the angular separation between the extra heavy quarks is used to remove the overlap between $t\bar{t}q\bar{q}$ ($q = b, c$) generated from the matrix element calculation and from parton-shower evolution in the $t\bar{t}$ +light samples is employed: matrix-element prediction is chosen over the parton-shower one when $\Delta R(q, \bar{q}) > 0.4$, else vice-versa.

Again a top quark mass of 172.5 GeV is assumed, and normalisation to the NNLO theoretical cross section is used (see 5.3.1)

W/Z +jets

Simulated samples of W/Z boson production in association with jets (W/Z +jets in the following) are generated with up to five additional partons using the ALPGEN v2.13 [?] LO generator and the CTEQ6L1 PDF set [?], interfaced to HERWIG v6.520 for parton showering and fragmentation.

“MLM matching” is used also here to avoid double-counting of partonic configurations between matrix-element calculation and parton showering.

The W +jets samples are generated separately for W +light jets, $Wb\bar{b}$ +jets, $Wc\bar{c}$ +jets, and Wc +jets, with the relative contributions normalized using the fraction of b -tagged jets in W +1-jet and W +2-jets data control samples [?], while the Z +jets samples are generated separately for Z +light jets, $Zb\bar{b}$ +jets, and $Zc\bar{c}$ +jets and normalized to the inclusive NNLO theoretical cross section [?].

Overlap between $W/Zq\bar{q}$ +jets ($q = b, c$) events generated from the matrix element calculation and those generated from parton-shower evolution in the W/Z +light jets samples is avoided via an algorithm analogous to the one used for $t\bar{t}$ Alpgen.

For the W +jets background, a normalisation from data for the shapes obtained from the simulation is derived since the simulation overestimates the number of W +jets events by up to $\sim 20\%$, depending on the jet multiplicity.

By exploiting the predicted asymmetry between W^+ +jets and W^- +jets production in p-p collisions [?], the total number of W +jets events in data ($N_W = N_{W^+} + N_{W^-}$), can be estimated based on the measured difference between the number of positively- and negatively-charged W bosons, $(N_{W^+} - N_{W^-})_{\text{meas}}$, and the asymmetry predicted from the simulation:

$$N_W = \left(\frac{N_{W^+} + N_{W^-}}{N_{W^+} - N_{W^-}} \right)_{\text{MC}} (N_{W^+} - N_{W^-})_{\text{meas}} \quad (5.1)$$

Events are categorised in terms of multiplicity of b and c jets and scale factors are derived using Equation 5.1. The fraction of W +light jets events is scaled accordingly in order to preserve the overall normalisation of the W +jets background before b tagging.

Other backgrounds

Simulated samples of single top quark backgrounds corresponding to the s -channel and Wt production mechanisms are generated with MC@NLO v4.01 [?, ?, ?] using the CT10 PDF set [?]. In the case of t -channel single top quark production, the ACERMC v3.8 LO generator [?] with the MRST LO** PDF set is used.

Simulated samples of $t\bar{t}$ produced in association with a W or Z boson ($t\bar{t}V$ ($V = W, Z$) in the following) are generated with the MADGRAPH v5 LO generator [?] and the CTEQ6L1 PDF set.

Samples of $t\bar{t}$ produced in association with a Higgs boson ($t\bar{t}H$ in the following) are generated with the PYTHIA 6.425 [?] LO generator and the MRST LO** PDF set [?],

assuming a Higgs boson mass of 125 GeV and considering the $H \rightarrow b\bar{b}$, $c\bar{c}$, gg , and W^+W^- decay modes.

Parton shower and fragmentation are modelled with HERWIG v6.520 [?] in the case of MC@NLO, with PYTHIA 6.421 in the case of ACERMC, and with PYTHIA 6.425 in the case of MADGRAPH. All these samples are generated assuming a top quark mass of 172.5 GeV. The single top quark samples are normalised to the approximate NNLO theoretical cross sections [?, ?] using the MSTW2008 NNLO PDF set, while the $t\bar{t}V$ samples are normalised to the NLO cross section predictions [?, ?]. The $t\bar{t}H$ sample is normalised using the NLO theoretical cross section and branching ratio predictions [?]. Finally, the diboson backgrounds are modelled using HERWIG with the MRST LO** PDF set, and are normalised to their NLO theoretical cross sections [?].

Signal samples

For vector-like T signals, samples corresponding to a singlet T quark decaying to Wb , Zt and Ht are generated with the PROTONS v2.2 LO generator [?, ?] using the MSTW2008 LO PDF set, and interfaced to PYTHIA for the parton shower and fragmentation.

For each decay channel (Wb , Zt and Ht) the branching ratio has been set to 1/3. Events are reweighted in order to reproduce any desired branching ratio configuration.

The predicted branching ratios in the weak-isospin singlet and doublet scenarios as a function of m_T are given in Table 5.2.

The m_T values considered range from 350 GeV to 850 GeV in steps of 50 GeV, with the Higgs boson mass assumed to be 125 GeV. All Higgs boson decay modes are considered, with branching ratios as predicted by HDECAY [?].

Signal samples are normalized to the approximate NNLO theoretical cross sections [?] using the MSTW2008 NNLO PDF set. The cross section values used are summarized in Table 5.3.

m_T (GeV)	$BR(T \rightarrow Wb)$	Singlet		$BR(T \rightarrow Wb)$	Doublet	
		$BR(T \rightarrow Zt)$	$BR(T \rightarrow Ht)$		$BR(T \rightarrow Zt)$	$BR(T \rightarrow Ht)$
350	0.545	0.116	0.338	0.000	0.255	0.745
400	0.513	0.139	0.348	0.000	0.285	0.715
450	0.502	0.158	0.341	0.000	0.316	0.684
500	0.497	0.173	0.330	0.000	0.343	0.657
550	0.495	0.185	0.321	0.000	0.365	0.635
600	0.494	0.194	0.312	0.000	0.383	0.617
650	0.494	0.202	0.304	0.000	0.399	0.601
700	0.494	0.208	0.298	0.000	0.411	0.589
750	0.494	0.214	0.292	0.000	0.422	0.578
800	0.494	0.218	0.288	0.000	0.431	0.569
850	0.494	0.222	0.284	0.000	0.439	0.561

Table 5.2: Branching ratios for T decay as a function of m_T as computed with PROTONS in the weak-isospin singlet and doublet scenarios.

m_T (GeV)	$\sigma(TT)$ (pb)	Scale uncertainties (pb)	PDF+ α_s uncertainties (pb)	Total uncertainty (pb)
350	5.083	+0.140/-0.285	+ 0.569/-0.488	+0.586/-0.565
400	2.296	+0.066/-0.130	+ 0.269/-0.221	+0.277/-0.257
450	1.113	+0.034/-0.063	+ 0.136/-0.107	+0.140/-0.125
500	0.5702	+0.0185/-0.0327	+ 0.0723/-0.0545	+0.0746/-0.0636
550	0.30545	+0.01040/-0.01769	+ 0.04012/-0.02889	+0.0414/-0.0339
600	0.1696	+0.0060/-0.0099	+ 0.0230/-0.0161	+0.0238/-0.0189
650	0.09707	+0.00359/-0.00571	+ 0.01363/-0.00936	+0.01410/-0.01097
700	0.05694	+0.00218/-0.00338	+ 0.00828/-0.00559	+0.00856/-0.00653
750	0.03411	+0.00135/-0.00204	+ 0.00513/-0.00343	+0.00530/-0.00400
800	0.02080	+0.00085/-0.00126	+ 0.00329/-0.00216	+0.00340/-0.00250
850	0.01287	+0.00054/-0.00079	+ 0.00215/-0.00138	+0.00222/-0.00159

Table 5.3: Theoretical cross section at NNLO for TT production as a function of m_T as computed by HATHOR, and scale and PDF uncertainties.

5.3.2 Multi-jet background

QCD production can pass the event selection in the electron channel as non-prompt electrons or as “fake” electrons, i.e. either electrons from photon conversions or mis-identified jets that left a high amount of energy in the electromagnetic calorimeter. For events in the muon channel the main contributions come from non-prompt leptons from semileptonic b - and c -hadron decays.

The contribution to the background from multi-jet events is estimated via data-driven methods, since simulation is not expected to predict this contribution with the desired level of accuracy. The technique used is called “Matrix Method” (MM in the following) [?].

5.4 Systematical uncertainties treatment

1005 **Preliminary search for $T\bar{T}$ pairs**
1006 **decaying to $Wb + X$**

1007

1008 **6.1 Boosted W reconstruction**

1009 **6.2 Control regions**

1010 **6.3 Event selection**

1011 **6.4 Systematics**

1013 Preliminary search for $T\bar{T}$ pairs
1014 decaying to $Ht + X$

1015

1016 7.1 Control regions

1017 7.2 Event selection

1018 7.3 Systematics

Results

1020

1021

8.1 Combination

1022

1023 Conclusions

1024

1030 **Search for $T\bar{T} \rightarrow Wb + X$ at $\sqrt{7}$ TeV**

1031

Bibliography

-
- [1] ATLAS Collaboration, *The ATLAS Experiment at the CERN Large Hadron Collider*, **JINST** **3** (2008) S08003.
- [2] J. Aguilar-Saavedra, *Identifying top partners at LHC*, **JHEP** **0911** (2009) 030, [arXiv:0907.3155 \[hep-ph\]](#).
- [3] S. P. Martin, *Extra vector-like matter and the lightest Higgs scalar boson mass in low-energy supersymmetry*, **Phys.Rev.** **D81** (2010) 035004, [arXiv:0910.2732 \[hep-ph\]](#).
- [4] D0 Collaboration Collaboration, S. Abachi and et al., *Search for High Mass Top Quark Production in $p\bar{p}$ Collisions at $\sqrt{s} = 1.8$ TeV*, **Phys. Rev. Lett.** **74** (Mar 1995) 2652, <http://link.aps.org/doi/10.1103/PhysRevLett.74.2422>.
- [5] CDF Collaboration Collaboration, F. Abe and et al., *Observation of Top Quark Production in $p\bar{p}$ Collisions with the Collider Detector at Fermilab*, **Phys. Rev. Lett.** **74** (1995) 2652, <http://link.aps.org/doi/10.1103/PhysRevLett.74.2626>.
- [6] ATLAS Collaboration, *Observation of a new particle in the search for the Standard Model Higgs boson with the ATLAS detector at the LHC*, **Phys.Lett.** **B716** (2012) 1–29, [arXiv:1207.7214 \[hep-ex\]](#).
- [7] CMS Collaboration, *The CMS experiment at the CERN LHC*, **JINST** **3** (2008) S08004.
- [8] ALICE Collaboration, *The ALICE experiment at the CERN LHC*, **JINST** **3** (2008) S08002.
- [9] LHCb Collaboration, *The LHCb experiment at the CERN LHC*, **JINST** **3** (2008) S08005.
- [10] L. Evans, P. Bryant (Eds.), *LHC Machine*, **JINST** **3** (2008) S08001.

- [11] M. Lamont, *The First Years of LHC Operation for Luminosity Production*, in *Proceedings of 4th International Particle Accelerator Conference (IPAC 2013)* (2013) .
- [12] ATLAS Collaboration.
<https://twiki.cern.ch/twiki/bin/view/AtlasPublic/LuminosityPublicResults>.
- [13] ATLAS Collaboration, *Studies of the performance of the ATLAS detector using cosmic-ray muons*, Eur. Phys. J. **C 71** (2011) 1593.
- [14] W. R., *Calorimetry*, Scientifica Acta **2 (1)** (2008) 1855.
- [15] ATLAS Collaboration, *Readiness of the ATLAS liquid argon calorimeter for LHC collisions*, Eur. Phys. J. **C 70** (2010) 723–753.
- [16] ATLAS Collaboration, *Readiness of the ATLAS Tile calorimeter for LHC collisions*, Eur. Phys. J. **C 70** (2010) 11931236.
- [17] ATLAS Collaboration, *Expected Performance of the ATLAS Experiment - Detector, Trigger and Physics*, [arXiv:0901.0512 \[hep-ex\]](https://arxiv.org/abs/0901.0512).
- [18] T. Cornelissen, M. Elsing, S. Fleischmann, W. Liebig, E. Moyse, and A. Salzburger, *Concepts, Design and Implementation of the ATLAS New Tracking (NEWT)*, Tech. Rep. ATL-SOFT-PUB-2007-007. ATL-COM-SOFT-2007-002, CERN, Geneva, Mar, 2007.
- [19] R. Frhwirth, *Application of Kalman filtering to track and vertex fitting*, *Nuclear Instruments and Methods in Physics Research Section A: Accelerators, Spectrometers, Detectors and Applications*, <http://www.sciencedirect.com/science/article/pii/0168900287908874>.
- [20] ATLAS Collaboration Collaboration, *Performance of primary vertex reconstruction in proton-proton collisions at $\sqrt{s}=7$ TeV in the ATLAS experiment*, Tech. Rep. ATLAS-CONF-2010-069, CERN, Geneva, Jul, 2010.
- [21] ATLAS Collaboration Collaboration, *Performance of the ATLAS Inner Detector Track and Vertex Reconstruction in the High Pile-Up LHC Environment*, Tech. Rep. ATLAS-CONF-2012-042, CERN, Geneva, Mar, 2012.
- [22] W. Lampl et al., *Calorimeter clustering algorithms: Description and performance*, ATL-LARG-PUB-2008-002 (2012) . <https://cdsweb.cern.ch/record/1099735>.
- [23] ATLAS Collaboration, *Electron performance measurements with the ATLAS detector using the 2010 LHC proton-proton collision data*, Eur.Phys.J. **C72** (2012) 1909, [arXiv:1110.3174 \[hep-ex\]](https://arxiv.org/abs/1110.3174).
- [24] E. Abat, J. Abdallah, T. Addy, P. Adragna, M. Aharrouche, et al., *Combined performance studies for electrons at the 2004 ATLAS combined test-beam*, JINST **5** (2010) P11006.
- [25] B. Acharya, J. Adelman, S. Adomeit, M. Aoki, B. Alvarez, F. Balli, W. Bell, K. Becker, K. Behr, D. Benjamin, E. Bergeas Kuutmann, C. Bernard, K. Black,

- 1093 S. Calvet, R. Camacho, Y. Coadou, G. Cortiana, N. Cooper-Smith, T. Cornelissen,
1094 M. Cristinziani, V. Dao, U. De Sanctis, C. Doglioni, F. Derue, K. Finelli, K. Grahn,
1095 J. Groth-Jensen, S. Head, A. Henrichs, D. Hirschbuehl, V. Kaushik, O. Kind,
1096 H. Khandanyan, A. Krasznahorkay, T. Kuhl, E. Le Menedeu, H. Lee, A. Lister,
1097 K. Loureiro, L. Miljovic, J. Morris, R. Moles Valls, O. Nackenhorst, D. Pelikan,
1098 M. Owen, M. Pinamonti, K. Rao, K. Rosbach, M. Rudolph, G. Salamanna,
1099 J. Schwindling, J. Searcy, E. Shabalina, K. Shaw, J. Sjolin, R. Soualah, S. Stamm,
1100 D. Ta, T. Theveneaux-Pelzer, E. Thompson, K. Uchida, L. Valery, M. Vreeswijk,
1101 C. Wasicki, I. Watson, K. Yau, J. Zhong, H. Zhu, and M. zur Nedden, *Object selection
1102 and calibration, background estimations and MC samples for the Winter 2013 Top
1103 Quark analyses with 2012 data*, Tech. Rep. ATL-COM-PHYS-2013-088, CERN,
1104 Geneva, Jan, 2013.
- 1105 [26] ATLAS Collaboration Collaboration, *Muon reconstruction efficiency in reprocessed
1106 2010 LHC proton-proton collision data recorded with the ATLAS detector*, Tech. Rep.
1107 ATLAS-CONF-2011-063, CERN, Geneva, Apr, 2011.
- 1108 [27] G. P. Salam, *Towards Jetography*, *Eur.Phys.J. C* **67** (2010) 637–686,
1109 [arXiv:0906.1833 \[hep-ph\]](#).
- 1110 [28] M. Cacciari, G. P. Salam, and G. Soyez, *The anti- k_t jet clustering algorithm*,
1111 *JHEP* **04** (2008) 063, [arXiv:0802.1189v2 \[hep-ph\]](#).
- 1112 [29] M. Cacciari and G. P. Salam, *Dispelling the N^3 myth for the k_t jet-finder*,
1113 *Phys. Lett. B* **641** (2006) 57, [arXiv:0512210v2 \[hep-ph\]](#).
- 1114 [30] M. Cacciari, G. P. Salam, and G. Soyez, *FastJet User Manual*,
1115 *Eur. Phys. J. C* **72** (2012) 1896, [arXiv:1111.6097 \[hep-ph\]](#).
- 1116 [31] ATLAS Collaboration, *Jet energy measurement with the ATLAS detector in
1117 proton-proton collisions at $\sqrt{s} = 7$ TeV*, *Eur. Phys. J. C* **73** (2013) 2304,
1118 [arXiv:1112.6426 \[hep-ex\]](#).
- 1119 [32] C. Cojocaru et al., *Hadronic calibration of the ATLAS liquid argon end-cap
1120 calorimeter in the pseudorapidity region $1.6 < |\eta| < 1.8$ in beam tests*,
1121 *Nucl. Instr. Meth. A* **531** (2004) 481, [arXiv:0407009 \[physics\]](#).
- 1122 [33] T. Barillari et al., *Local hadronic calibration*, ATL-LARG-PUB-2009-001 (2009) .
1123 <https://cds.cern.ch/record/1112035>.
- 1124 [34] ATLAS Collaboration, *Commissioning of the ATLAS high-performance b-tagging
1125 algorithms in the 7 TeV collision data*, ATLAS-CONF-2011-102 (2011) .
1126 <https://cds.cern.ch/record/1369219>.
- 1127 [35] ATLAS Collaboration, *Measurement of the b-tagging efficiency in a sample of jets
1128 containing muons with 5 fb^{-1} of data from the ATLAS detector*,
1129 ATLAS-CONF-2012-043 (2012) . <https://cdsweb.cern.ch/record/1435197>.

- 1130 [36] ATLAS Collaboration, *Performance of Missing Transverse Momentum Reconstruction*
1131 *in Proton-Proton Collisions at 7 TeV with ATLAS*, Eur. Phys. J. C **72** (2012) 1844,
1132 [arXiv:1108.5602 \[hep-ex\]](#).